Independent tephrochronological evidence for rapid and synchronous oceanic and atmospheric temperature rises over the Greenland stadial-interstadial transitions between ca. 32 and 40 ka b2k

Sarah M.P. Berben [a, *], Trond M. Dokken [b], Peter M. Abbott [c, d, 1], Eliza Cook [e], Henrik Sadatzki [a, b, f], Margit H. Simon [b], Eystein Jansen [a, b]

[a] Department of Earth Science and Bjerknes Centre for Climate Research, University of Bergen, 5007, Bergen, Norway
[b] NORCE Norwegian Research Centre and Bjerknes Centre for Climate Research, 5007, Bergen, Norway
[c] School of Earth and Ocean Sciences, Cardiff University, Cardiff, CF10 3AT, United Kingdom
[d] Institute of Geological Sciences and Oeschger Center for Climate Research, University of Bern, 3012, Bern, Switzerland
[e] Physics of Ice, Climate and Earth, Niels Bohr Institute, University of Copenhagen, 2200, Copenhagen, Denmark
[f] Research School of Earth Sciences, Australian National University, Canberra, ACT, 2601, Australia

ARTICLE INFO

ABSTRACT

Understanding the dynamics that drove past abrupt climate changes, such as the Dansgaard-Oeschger (DO) events, depends on combined proxy evidence from disparate archives. To identify leads, lags and synchronicity between different climate system components, independent and robust chronologies are required. Cryptotephrochronology is a key geochronological tool as cryptotephra horizons can act as isochrons linking disparate and/or distant records. Here, we investigated marine sediment core MD99-2284 from the Norwegian Sea to look for previously identified Greenland ice core cryptotephra horizons and define time-parallel markers between the archives. We explored potential secondary transport and depositional mechanisms that could hamper the isochronous integrity of such horizons. We identified six cryptotephra layers of which four correlate to previously known Greenland ice core horizons. None of those were identified in other marine cores and thus, this study contributes greatly to the North Atlantic tephra framework tripling the original amount of existing isochrons between ca. 25 and 60 ka b2k. The latter allow a synchronization between MD99-2284 and the Greenland ice cores between ca. 32 −40 ka b2k, which is, in the North Atlantic, the shortest time-interval during the Last Glacial Period to be constrained by four independent tephra isochrons. These findings provide essential tephra-based evidence for synchronous and rapid oceanic and atmospheric temperature rises during the Greenland Stadial-Interstadial transitions. Furthermore, it enables us to estimate the average peak-duration of interstadial temperature overshoots at approximately 136 years. As such, this well-targeted high-resolution investigation successfully demonstrates the use of cryptotephra for geochronological purposes in the marine realm.

1. Introduction

Tephrochronology is considered to be a key correlation tool for establishing precise synchronization of disparate and/or distant climate archives (e.g. Grönvold et al., 1995; Rasmussen et al., 2003; Wastegård et al., 2006; Lowe et al., 2008; Brendryen et al., 2010; Lowe, 2011; Blockley et al., 2012; Davies et al., 2012, 2014; Wastegård and Rasmussen, 2014; Davies, 2015). When geochemically unique volcanic ash (tephra) is ejected during an eruption and rapidly deposited, it can be traced in and between different depositional realms and subsequently, it has the potential to act as an isochron (e.g. Lowe, 2011; Davies, 2015). Isochrons, or time-parallel markers, are used for the independent correlation of climatic sequences which helps to assess the relative timing and phasing of

* Corresponding author.
   E-mail addresses: sarah.berben@uib.no (S.M.P. Berben), trdo@norceresearch.no (T.M. Dokken), peter.abbott@climate.unibe.ch (P.M. Abbott), elizacook@nbi.ku.dk (E. Cook), Henrik.Sadatzki@anu.edu.au (H. Sadatzki), msim@norceresearch.no (M.H. Simon), Eystein.Jansen@uib.no (E. Jansen).
   [1] Now at: Climate and Environmental Physics and Oeschger Centre for Climate Change Research, University of Bern, CH-3012 Bern, Switzerland.

past events (e.g. Lowe, 2011; Davies, 2015). Determining the phasing of events is crucial for understanding the dynamics controlling abrupt climate changes such as the Dansgaard-Oeschger (DO)-events. These events were recorded during the Last Glacial Period in the Greenland ice cores (Bond et al., 1993; Dansgaard et al., 1993) as well as in the North Atlantic marine realm (e.g. Curry and Oppo, 1997; Dokken and Jansen, 1999) reflecting atmospheric conditions over the Greenland ice-sheet and oceanic variability in the North Atlantic, respectively. However, to obtain a full picture of the fluctuations in, and/or interactions between, the atmosphere and ocean during these events and therefore, to fully comprehend the dynamics involved, it is crucial to combine and compare the disparate climate archives on independent age models (e.g. Davies et al., 2012). As such, an independent method to correlate these records and test the synchronous or non-synchronous responses (leads/lags) to climatic fluctuations is required and can be provided by tephrochronology.

Within the field of tephrochronology, the recent expansion in the identification of cryptotephra horizons (i.e. low-concentration tephra layers, invisible to the naked eye) offers an increased potential for correlation and integration of different climate archives (Davies, 2015). The Greenland ice cores have been screened for their cryptotephra content over selected intervals (e.g. over rapid climate transitions and around notable volcanic events) between ca. 25 and 45 ka b2k (Davies et al., 2008, 2010; Bourne et al., 2015). Bourne et al. (2015) presents a unique insight into North Atlantic volcanism for that period through a significantly enhanced Greenland ice core tephrochronological framework beyond the previously known visible layers (Grönvold et al., 1995; Zielinski et al., 1996). The enhancement of the framework is of crucial importance for the synchronization of the Greenland ice cores with other palaeoclimatic records, especially where geochemically unique deposits constrain the transitions between Greenland Stadials (GS) and Greenland Interstadials (GI) characterizing DO-events. If the same horizons are traced in distal North Atlantic marine records, these deposits form isochrons that can be used as time-parallel markers linking the different archives.

Correlating tephra horizons depends on robust investigations of the geochemical composition of individual grains within each deposit. Additionally, such information is also useful for assessing depositional processes for marine cryptotephras. In particular, when tephra horizons of multiple eruptions from the same volcano are deposited over a short time-frame, the stratigraphic separation of these events might be hampered. For example, Bourne et al. (2013) demonstrates that the Faroe Marine Ash Zone III (FMAZ III) deposit, once considered a keystone DO-8 time-parallel marker between the Greenland ice cores (Davies et al., 2010) and a number of marine records (Rasmussen et al., 2003; Wastegård et al., 2006), is a far more complex ash zone than previously thought. The Greenland ice cores record 14 separate Grímsvötn volcanic eruptions during GS-9 and GI-8 which all fall within the broad compositional range of FMAZ III (Bourne et al., 2013). In order to use one of these ice core tephra horizons as a time-parallel marker, it is necessary to also separate them in the marine realm, which requires a detailed shard profile and geochemical investigation of high sedimentation-rate marine cores (Bourne et al., 2013; Griggs et al., 2014).

For the North Atlantic realm, recent intensive studies focusing on cryptotephra (e.g. Brendryen et al., 2010; Griggs et al., 2014; Abbott et al., 2016, 2018a) resulted in an enhanced North Atlantic marine tephra framework for Marine Isotope Stage (MIS) 2−3 (i.e. ca. 25 to 60 ka b2k) (Abbott et al., 2018a). Nonetheless, despite this significant contribution demonstrating the potential for detecting cryptotephra layers in marine records, the actual number of

isochronous deposits in the North Atlantic (ca. 14) (Abbott et al., 2018a) is profoundly lower than those recorded in the Greenland ice cores (ca. 100) (Bourne et al., 2015). Although several of those North Atlantic deposits possess the potential to act as ice-marine time-parallel markers, only the well-known FMAZ II and NAAZ II horizons have, thus far, been identified in both marine and ice core records between ca. 25 and 60 ka b2k (Abbott et al., 2018a). The low number of existing isochrons (2) and the discrepancy between the numbers of tephra horizons recorded in the different archives is most likely related to many challenges specific to the marine realm. Firstly, detecting low-concentration cryptotephra horizons in marine sediments requires an intensive approach including a sequence of extraction techniques (Davies, 2015). Secondly, various secondary transport and deposition mechanisms can compromise the isochronous nature of marine tephra horizons (e.g. Griggs et al., 2014; Davies, 2015; Abbott et al., 2018b).

The instantaneous deposition of tephra is a fundamental principle of tephrochronology and thus, it is imperative to fully examine if any processes have delayed transportation and/or reworked shards after initial deposition (e.g. Austin et al., 2004; Brendryen et al., 2010; Griggs et al., 2014; Abbott et al., 2011, 2018b). Previous studies demonstrated the added value of assessing the co-variance of ice rafted debris (IRD) and shard concentrations to detect if tephra horizons were transported by ice (Brendryen et al., 2010; Griggs et al., 2014; Abbott et al., 2018b). Employing high-resolution down-core concentration profiles has been shown to be useful for evaluating the influence of sediment reworking through bottom currents and bioturbation (Abbott et al., 2013, 2014; Griggs et al., 2014). A classification scheme for glass shard deposits, recently developed by Abbott et al. (2018b), uses such indicators to classify deposits with common characteristics and explore the influence of primary and secondary processes. These additional steps enable one to disentangle the complex interplay of processes that were active in the North Atlantic during the Last Glacial Period and aid the assessment of the integrity of a deposit as an isochronous marker. Abbott et al. (2018b) additionally assessed the spatial distribution of cryptotephra in the North Atlantic and concluded that areas south and east of Iceland possess the highest potential for preserving isochronous horizons that may expedite the synchronization of palaeoclimatic records.

Here, our overall aim is to stratigraphically resolve individual tephra layers within marine sediment core MD99-2284 that can be correlated with common horizons previously identified in the Greenland ice cores (Bourne et al., 2013, 2015). We conducted a well-targeted high-resolution investigation of marine cryptotephra horizons between DO-5 and DO-9 (i.e. ca. 32−40 ka b2k) and applied the protocol for identification, characterization and evaluating depositional controls for marine cryptotephras outlined in Abbott et al. (2018b). MD99-2284, retrieved from the Nordic Seas, was selected due to its high sedimentation-rate, location and the results of prior studies of the sequence. In particular, previous studies presented an age model based on a tuning approach (i.e. an alignment of marine core parameters to ice core parameters) (see 2.1.2.) (Dokken et al., 2013; Sadatzki et al., 2019). Additionally, a wide variety of palaeoclimatic proxy records has already been reconstructed with an exceptionally high temporal resolution (i.e. decadal to centennial) (see 2.1.2.) (Dokken et al., 2013; Sadatzki et al., 2019). If successful in our initial aim, we intend to 1) synchronize marine sediment core MD99-2284 to the Greenland ice cores based on independent cryptotephra time-parallel markers (i.e. isochrons) and thereby, independently verify the existing tuning method and refine the core's age model, 2) place the marine and ice core proxy records on an integrated chronological framework that constrains rapid climatic events, which further allows for a detailed estimation of the timing and phasing of abrupt events,

and 3) improve the existing North Atlantic tephra framework through the discovery of previously unidentified isochrons.

2. Material & methods

2.1. Material

2.1.1. Greenland ice core tephra framework

To construct the most comprehensive MIS 3 tephrochronological framework for Greenland, Bourne et al. (2015) employed an intensive ice sampling methodology for four deep ice cores: North Greenland Ice Core Project (NGRIP) (2917 m asl), North Greenland Eemian Ice Drilling (NEEM) (2484 m asl), Greenland Ice Core Project (GRIP) (3230 m asl) and DYE-3 (2480m asl) (Fig. 1). With the discovery of 73 new tephra deposits, in addition to the previously published 26 horizons (Davies et al., 2010; Bourne et al., 2013), the resulting Greenland ice core tephra framework highlighted the nature and unexpected high frequency of volcanic activity in the North Atlantic region. Several of the tephra horizons were identified in close stratigraphic proximity to sharp transitions that mark abrupt climate events characterizing the Last Glacial Period (i.e. DO-events). Their stratigraphic positions make these tephra layers key horizons to target and locate within the marine realm (Bourne et al., 2015). For every tephra horizon, the authors assigned an independent age that was derived from the Greenland Ice Core Chronology (GICC05) (Andersen et al., 2006; Svensson et al., 2006). This Greenland ice core tephra framework strongly increases the opportunities for independent synchronizations between disparate and/or distant climate archives.

Here, the focus lies on those Greenland ice core horizons with strong isochron potential that constrain rapid climatic changes between ca. 32 and 40 ka b2k: 1) the tephra horizons deposited during GI-5, GS-6, GI-6 and GI-7 and 2) the closely spaced eruptive events recorded between GI-8 and GS-10 (Table 1). The geochemical compositions of those layers were compared to the best available published data to attribute each horizon to the most likely volcanic source (Bourne et al., 2015). The different source volcanoes can be traced back to Iceland and, except for one dacitic/rhyolitic (Hekla) horizon, all tephra layers of interest have a basaltic composition (Table 1). In particular, the layers identified during both GI-5 and GI-6 originate from Kverkfjöll (Iceland) but differences in their Al_2O_3 and TiO_2 concentrations allow them to be distinguished one from another. The horizon during GS-6 was attributed to Katla (Iceland) and the closely spaced eruptions between GI-8 and GS-10 are, apart from one, all ascribed to Grímsvötn (Table 1). Discriminating between the geochemical compositions of these deposits within the same stratigraphic unit in the Greenland ice core record is challenging (Bourne et al., 2013, 2015) and even more so in the marine realm (e.g. Griggs et al., 2014; Abbott et al., 2016, 2018a). However, due to very small differences in their TiO_2 content, it is possible to separate the horizons into different subgroups despite limited stratigraphic separation (Bourne et al., 2013, 2015).

2.1.2. Marine sediment core MD99-2284

Here, we focus on core MD99-2284 (62°22.48 N, 0°58.81 W) retrieved during the MD114/IMAGES V cruise aboard R/V Marion Dufresne (IPEV) (Dokken et al., 2013) (Fig. 1). This core was taken in the Nordic Seas on the northeastern flank of the Faeroe-Shetland channel at a water depth of 1500 m (Dokken et al., 2013).

MD99-2284 is of particular interest as the core site is located along the pathway of inflowing warm Atlantic water into the Nordic Seas via the North Atlantic Current (Fig. 1). Hence, this core was retrieved from an excellent location to capture information with respect to the MIS 3 fluctuations of oceanography and sea ice cover. The latter was confirmed by the reconstructed proxy records of near-surface temperature (SST), planktic and benthic foraminiferal isotopes (Dokken et al., 2013) as well as sea ice biomarkers (Sadatzki et al., 2019) that all preserve a record of the GS-GI transitions between DO-5 and DO-9. These marine proxy records
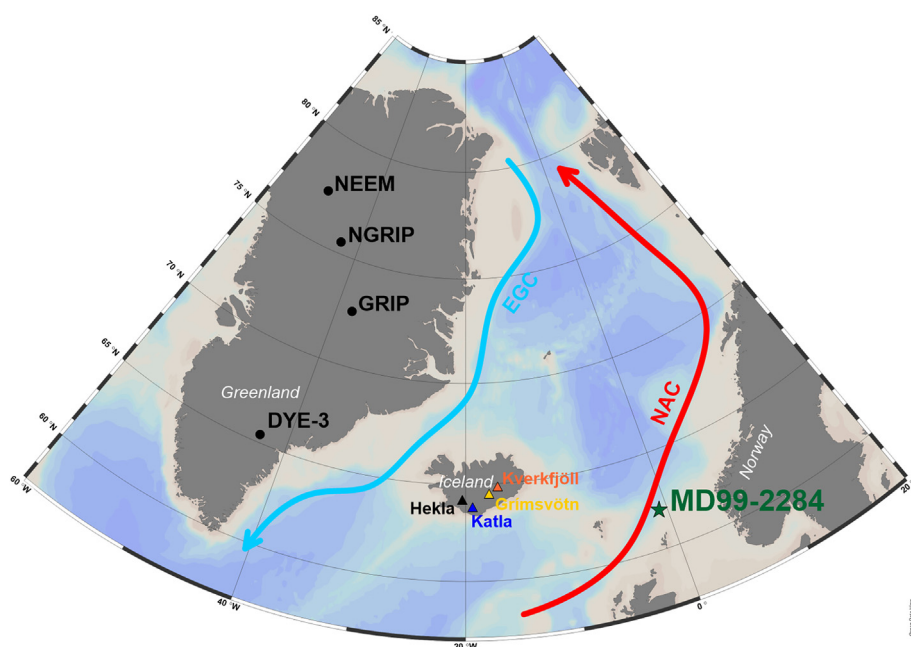

Fig. 1. Map of the northern North Atlantic region presenting the locations of studied core material and Icelandic volcanic systems. Marine sediment core MD99-2284 (62°22.48 N, 0°58.81 W; 1500 m water depth) (green star). Greenland ice cores NEEM, NGRIP, GRIP and DYE-3 (black dots). Icelandic volcanic systems (triangles): Kverkfjöll (orange), Grímsvötn (yellow), Katla (blue) and Hekla (black). Surface currents indicate the warm Atlantic water inflow northwards and returning southwards outflow of cold Polar water. NAC = North Atlantic Current. EGC = East Greenland Current. Map was made with Ocean Data View (Schlitzer, 2018). (For interpretation of the references to color in this figure legend, the reader is referred to the Web version of this article.)

Table 1
Summary of key tephra horizons previously identified in the Greenland ice core tephra framework (Bourne et al., 2013, 2015) that are targeted in this study. For each horizon, the following information is provided: label (including depth), climatic event, geochemistry after Le Bas et al. (1986) (TB = Tholeiitic Basalt, TAB = Transitional Alkali Basalt, Da = Dacite, R = Rhyolite) and most likely volcanic source. In addition, the identified tephra horizons of MD99-2284 are added for each stratigraphically fitting Greenland ice core tephra layer.

Greenland ice core tephra layer			Climatic event	Geochemistry	Volcanic source	Reference	Stratigraphically fitting MD99-2284 Horizons
NGRIP	NEEM	GRIP					
1950.50 m	1689.25 m	–	GI-5	TB	Kverkfjöll	Bourne et al. (2015)	A, B, C
1952.15 m	1690.35 m	–	GS-6	TAB	Katla	Bourne et al. (2015)	A, B, C
1954.70 m	–	–	GS-6	TAB	Katla	Bourne et al. (2015)	A, B, C
1973.16 m	1702.40 m	–	GI-6	TB	Kverkfjöll	Bourne et al. (2015)	A, B, C
2009.15 m	–	–	GI-7	Da/R	Hekla	Bourne et al. (2015)	D
2064.35 m	1755.60 m	2195.45 m	GI-8	TB	Grímsvötn	Bourne et al. (2013, 2015)	E, F
2065.65 m	–	–	GI-8	TB	Grímsvötn	Bourne et al. (2013, 2015)	E, F
2065.80 m	–	–	GI-8	TB	Grímsvötn	Bourne et al. (2013, 2015)	E, F
2066.95 m	1757.10 m	2197.45 m	GI-8	TB	Grímsvötn	Bourne et al. (2013, 2015)	E, F
2071.50 m	1759.85 m	2201.50 m	GS-9	TB	Grímsvötn	Bourne et al. (2013, 2015)	E, F
2073.15 m	–	–	GS-9	TB	Grímsvötn	Bourne et al. (2013, 2015)	E, F
2078.01 m	1764.25 m	2207.00 m	GS-9	TB	Grímsvötn	Bourne et al. (2013, 2015)	E, F
2078.37 m	–	–	GS-9	TB	Grímsvötn	Bourne et al. (2013, 2015)	E, F
2078.97 m	–	–	GS-9	TB	Grímsvötn	Bourne et al. (2013, 2015)	E, F
2079.40 m	–	–	GS-9	TB	Grímsvötn	Bourne et al. (2013, 2015)	E, F
2085.80 m	–	–	GS-9	TAB	Katla	Bourne et al. (2013, 2015)	E, F
2100.65 m	–	–	GS-10	TB	Grímsvötn	Bourne et al. (2013, 2015)	F
2101.55 m	–	–	GS-10	TB	Grímsvötn	Bourne et al. (2013, 2015)	F
2103.98 m	1780.20 m	2227.15 m	GS-10	TB	Grímsvötn	Bourne et al. (2013, 2015)	F

expose the different conditions during GS and GI intervals as well as the abruptness of the GS-GI transitions in great detail due to the marine core's exceptionally high sedimentation-rates (ca. 50−400 cm/ka) (Dokken et al., 2013; Sadatzki et al., 2019). The temporal resolution varies between 2.5 and 20 years per cm allowing for a tephra investigation on an extremely high-resolution (i.e. on a decadal time-scale).

Building on a previously published age model for MD99-2284 (Dokken et al., 2013), a more detailed version was presented for the DO-5 to DO-9 time-interval by Sadatzki et al. (2019). These age models were constructed by aligning transitions in anhysteretic remanent magnetization (ARM), measured along MD99-2284, with similar fluctuations (i.e. DO-signals) in NGRIP $\delta^{18}O$ (Andersen et al., 2004, 2006; Seierstad et al., 2014). This alignment was based on the work of Kissel et al. (1999) who indicated that the oscillations in magnetic properties in the North Atlantic change in phase with Greenland ice core $\delta^{18}O$ records. Moreover, distinct temperature rises in the SST record of MD99-2284, parallel to the ARM increases, were aligned to the stadial-interstadial warming transitions in the NGRIP $\delta^{18}O$ record (Sadatzki et al., 2019). Based on change point analysis of the proxy records, Sadatzki et al. (2019) used 11 tie-points and linear interpolation between those for the age model of MD99-2284 (Fig. 2a). This tuning placed the marine sediment core depth-scale on the Greenland Ice Core Chronology (GICC05) (Andersen et al., 2006; Svensson et al., 2006; Seierstad et al., 2014) (Fig. 2a). The tuning approach of Sadatzki et al. (2019) was supported by the positions of the Laschamp and Mono Lake geomagnetic excursions as well as by the identification of a tephra horizon (i.e. MD99-2284_3040−3041 cm) that has been linked to the NGRIP 2065.65 m horizon published by Bourne et al. (2013). These separate lines of evidence argue for a strong chronological control on the DO-5 to DO-9 time-interval. Thus, the existing chronology of MD99-2284 adds to the value of this marine sediment core to be used for a detailed and high-resolution cryptotephra investigation.

To determinate the depth-intervals where the key tephras from the Greenland ice cores (see 2.1.1.) could be located, the most recent age model of Sadatzki et al. (2019) was used. A wider interval (i.e. ca. 150 years above and below the selected tephra horizons) was chosen to account for uncertainties in the age-depth model. Furthermore, the tephra horizon identified by Sadatzki et al. (2019)

was recorded within a low-resolution (every 4 cm) tephra investigation between 3020 and 3180 cm. As this depth-interval stratigraphically corresponds to the separated horizons in the ice cores associated with the marine FMAZ III deposit (Bourne et al., 2013) (see 2.1.1.), a more detailed investigation (i.e. high-resolution quantification of shards) of this stratigraphic unit was executed in order to assess whether the stratigraphically separated horizons in the ice cores can be resolved in the marine realm.

Subsequently, a cryptotephra investigation was executed for the following four selected depth-intervals: 1) 2108−2148 cm, 2) 2270−2350 cm, 3) 2645−2700 cm, and 4) 3020−3180 cm, representing the GS-6/GI-5, GS-7/GI-6, GS-8/GI-7 and GS-9/GI-8 transitions, respectively (see numbered boxes in Fig. 2). Depending on the composition of the Greenland ice core tephra horizons that were targeted, the tephra shard quantification was focused on basaltic shards for depth-intervals one, two and four and on rhyolitic shards for depth-interval three (Fig. 2).

2.2. Methods

The methodology for the cryptotephra investigation in this study follows the protocol outlined by Abbott et al. (2018b) building upon previous studies of marine and terrestrial sequences (e.g. Pilcher and Hall, 1992; Turney, 1998; Blockley et al., 2005; Abbott et al., 2011, 2013; Griggs et al., 2014). The tephra shard concentrations were initially counted at a low-resolution (i.e. non-contiguously for every 2−4 cm) and recounted at a higher resolution (i.e. contiguously for every 1 cm) around identified shard concentration peaks.

2.2.1. Tephra shard concentrations

The selected material underwent several separation steps in order to isolate tephra from other materials and further separate grains based on grain-size and density fractions of interest.

For the extraction of glass shards, sub-samples of ca. 0.5 g were freeze-dried and homogenized. Further, to remove any carbonate material, they were immersed in 6 ml of dilute (10%) hydrochloric acid (HCl) for ca. 24 h. Then, they were sieved using 125 μm and 80 μm stainless steel test sieves and a 25 μm nylon mesh sieve to separate the glass shards in three recommended size fractions
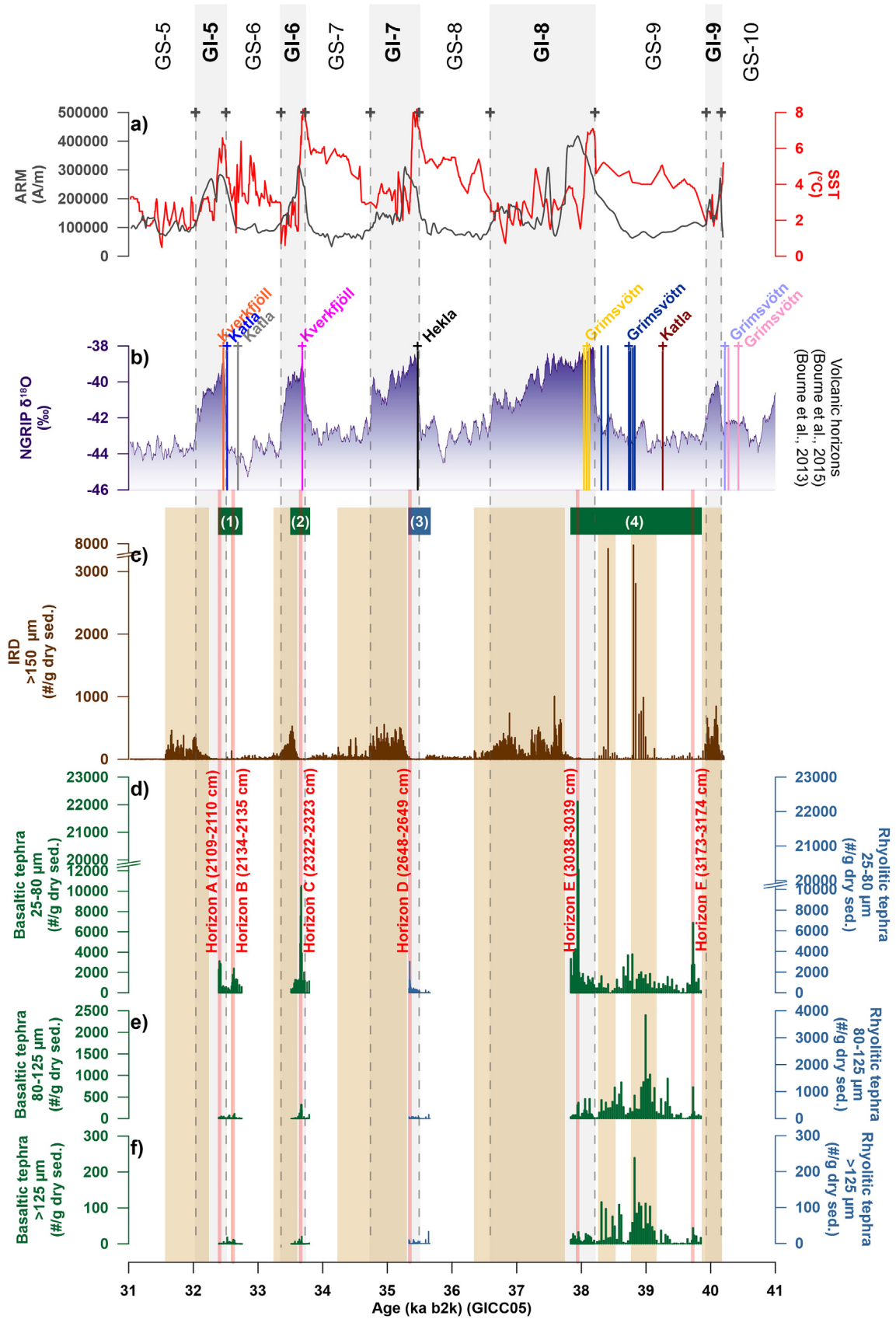
Fig. 2. Tephra shard concentration profiles and climatic parameters of MD99-2284 within the studied time-interval (ca. 32−40 ka b2k). The light grey highlighted areas represent the Greenland Interstadials (GI) 5−9. In this figure, all MD99-2284 results are plotted versus age (ka b2k) on the GICC05 time-scale based on the age model presented in Sadatzki et al. (2019). Dark grey crosses and dotted lines indicate 10 out of 11 ARM/SST-based tuning-points used for the latter age model. a) Anhysteretic remanent magnetization (ARM) (dark grey) and reconstructed near-surface temperature based on planktic foraminiferal assemblages (SST) (red) (Dokken et al., 2013). b) NGRIP ice core δ18O plotted as 25 point

(Abbott et al., 2018b).

The separation of the smallest size fraction (i.e. 25-80 μm) is important as it enhances the identification of fine-grained deposits (Davies, 2015). This fraction was separated into different density fractions using a heavy liquid separation technique originally developed for terrestrial sediments (Hodder and Wilson, 1976; Turney, 1998; Blockley et al., 2005). Sodium polytungstate was prepared to create heavy liquids of both 2.3 gcm^{-3} and 2.5 gcm^{-3}, which was then used to isolate the rhyolitic and basaltic glass shards in density fractions of 2.3 gcm^{-3} to 2.5 gcm^{-3} and >2.5 gcm^{-3}, respectively. All >2.5 gcm^{-3} fractions potentially containing basaltic glass shards underwent magnetic separation to aid in their isolation and identification as it was previously demonstrated to be a valuable additional step within marine cryptotephra studies in the North Atlantic (Griggs et al., 2014; Abbott et al., 2018b). From the oven-dried >2.5 gcm^{-3} fraction, the paramagnetic basaltic material was separated from the non-magnetic minerogenic material using a Frantz Magnetic separator and the settings of Griggs et al. (2014) (i.e. tilt = −15°, slope = 22.5°, current = 0.85 nA).

Finally, all the different size fractions from each sample were mounted separately in Canada Balsam on microscope slides and inspected using optical light microscopy for their tephra shard concentrations (#/g dry sediment) by identifying basaltic (brown-colored) and rhyolitic (transparent) glass shards.

2.2.2. Ice rafted debris concentrations

To obtain a better understanding of secondary transport mechanisms, an IRD record was also constructed. Such a record has proven to be important when ice-rafting processes might compromise the integrity of tephra layers in high-latitude settings during glacial periods (Brendryen et al., 2010; Griggs et al., 2014; Abbott et al., 2018b). In particular, tephra shards deposited onto ice-sheets can be transported to marine core sites after calving and rafting of icebergs. The ice-rafting might impart a temporal delay between eruption and final deposition of several millennia and thereby, hamper the isochronous nature of tephra deposits (Brendryen et al., 2010). Depending on the ice-sheet calving time, the ice-rafting might deposit shards larger than those typically associated with air fall as well as a compilation of tephra originating from different volcanic eruptions. The latter results in a heterogeneous geochemical composition (Ruddiman and Glover, 1972; Lackschewitz and Wallrabe-Adams, 1997; Brendryen et al., 2010; Abbott et al., 2011). Hence, in addition to the geochemical composition of a tephra horizon, an important criterion to recognize ice-rafted tephra horizons is a co-varying IRD record (Lackschewitz and Wallrabe-Adams, 1997; Davies et al., 2014). The IRD concentrations (#/g dry sediment) were calculated by counting the IRD fragments (>150 μm), excluding any volcanic material, continuously for every 2 cm.

2.2.3. Geochemical analysis of cryptotephra deposits

Samples showing a maximum peak in tephra shard concentrations alongside no increased IRD input for the same sample depth were chosen for geochemical analysis. Prior to embedding the sample material in epoxy resin on frosted microprobe slides (24 × 48 mm) the same separation steps as previously described (see 2.2.1.) were applied. Subsequently, the epoxy resin was ground using silicon carbide paper to expose the surface of the glass shards

and polished with diamond polycrystalline suspension (3, 1 and 0.5 μm) and alumina powder to provide an unscratched surface for geochemical analysis (Griggs et al., 2014; Abbott et al., 2018b).

The geochemical characterization of individual glass shards was conducted at the Tephrochronological Analytical Unit at the University of Edinburgh using electron-probe microanalysis (EPMA). A Cameca SX-100 electron microprobe with five vertical wavelength dispersive spectrometers was operated over several analytical periods to measure oxide concentrations (wt. %) of ten major elements. All measurements were performed using the operating conditions outlined in Hayward (2012). Depending on the grain-size of the samples, either a 3 or 5 μm beam diameter was used. To determine the instrumental drift within analytical sessions as well as assess the precision and accuracy of analysed samples, the secondary standards of Lipari Obsidian and BCR2g basalt were analysed at the beginning and end of each day. From each sample, ca. 20 individual shards were analysed to obtain a geochemical characterization that allows for a thorough assessment of the isochronous nature of the respective tephra layer. All analyses with total oxide values <97% were rejected. In order to compare the new marine tephra data of this study with the previously published data from the Greenland ice core tephra framework (Bourne et al., 2013, 2015), the major element data were normalized to an anhydrous basis (i.e. 100% total oxides). The latter was done due to the different levels of post-depositional hydration that might occur between the different depositional environments (Abbott et al., 2011; Pearce et al., 2014). In particular, tephra shards preserved in the marine realm are known to be susceptible to fluctuating levels of post-depositional hydration (Wallrabe-Adams and Lackschewitz, 2003; Abbott et al., 2011). The full geochemical results and secondary standard data are provided in the Supplementary Data.

In order to determine potential matches between marine tephra deposits and Greenland ice core tephra horizons, the geochemical populations of stratigraphically fitting horizons were both visually and statistically compared. The similarity coefficient (SC) was used to compare major elements from different datasets by calculating their similarity (Borchardt et al., 1972; Begét et al., 1992; Hunt et al., 1995). As the lower precision of low concentration elements might influence the coefficient, elements with concentration below 1 wt. % were not considered (Hunt et al., 1995). Consequently, only seven major elements were taken into consideration for the SC calculation. According to Begét et al. (1992), values between 0.95 and 1 indicate that both datasets are identical. However, here we have followed the recommendation of Abbott et al. (2018a) who applied a stricter approach as for some of the Icelandic centers values higher than 0.95 might just indicate a common source and values higher than 0.97 are more indicative of an identical geochemical composition. Another statistical parameter used was statistical distance (D^2) developed by Perkins et al. (1995, 1998). This method uses the Euclidian distance between samples to determine the difference between the geochemical datasets. The critical value for testing D^2 values using 10 major elements, at the 99% confidence interval, is 23.21 (10 degrees of freedom). D^2 values higher than the critical value indicate that the datasets being compared can be considered different and thus, the hypothesis that the samples are identical can be rejected (Pearce et al., 2008).

---

moving average (purple) (Andersen et al., 2004, 2006; Seierstad et al., 2014) and volcanic horizons (vertical bars) and their volcanic systems identified by Bourne et al. (2013, 2015). c) Ice rafted debris (IRD) concentrations counted in the >150 μm size fraction (brown). The light brown shaded areas represent intervals with increased input of IRD. d-f) Basaltic (green) and rhyolitic (blue) tephra shard concentrations counted in 25−80 μm, 80−125 μm and >125 μm size fractions for the selected depth-intervals: (1) 2108−2148 cm, (2) 2270−2350 cm, (3) 2645−2700 cm and (4) 3020−3180 cm. These depth-intervals are indicated in numbered green and blue boxes for the quantification of basaltic and rhyolitic concentrations, respectively. Each peak concentration is highlighted by a soft red line and labeled as Horizon A-F (marine core depth). (For interpretation of the references to color in this figure legend, the reader is referred to the Web version of this article.)

3. Tephrostratigraphy

The new tephrostratigraphy is presented here through descriptions of the high-resolution tephra shard and IRD concentration profiles including the different glass shard size fractions versus the chronology of Sadatzki et al. (2019) (Fig. 2; see 3.1.). The identified tephra horizons are assessed for their potential isochronous nature following the assessment protocol outlined by Abbott et al. (2018b). Subsequently, to determine if the selected horizons can also act as independent time-parallel markers, the geochemical signatures are presented and compared with existing geochemical data from stratigraphically similar Greenland ice core tephra horizons (Bourne et al., 2013, 2015) (see 3.2.).

3.1. High-resolution shard concentrations

In general, there is a pronounced difference between the tephra shard profiles of GI-5 to GI-7 and the tephra concentrations of GI-8/GS-9 (Fig. 2d—f). Within the coarser size fractions, the shard concentrations of GI-5/GS-6 and GI-7/GS-8 hardly record any tephra (Fig. 2e—f) despite a clear observation of, respectively, two and one concentration peak(s) in the 25—80 μm fraction (Fig. 2d). For GI-6/GS-7, one distinct tephra peak is recorded in all size fractions around the same depth, albeit slightly offset between the different size fractions (Fig. 2d—f). During GI-8/GS-9, however, the shard profiles of all three size fractions show a profoundly different pattern. In particular, compared to GI-8, the coarser-grained size fractions (i.e. >125 μm and 80—125 μm) show throughout GS-9 much higher concentrations including multiple concentration peaks (Fig. 2e—f). Yet, the fine-grained fraction (i.e. 25-80 μm) records one pronounced concentration peak during GI-8 and the most distinctive of GS-9 towards the end of the selected depth-interval (Fig. 2d).

The IRD record generally displays high concentrations during the interstadials and low concentrations during the stadials (Fig. 2c). However, an extremely high IRD input is recorded during GS-9. These periods of increased IRD are indicative that icebergs reached the core site and potentially deposited tephra shards that are older in age compared to their current stratigraphic position in the sediment core (Brendryen et al., 2010; Griggs et al., 2014; Abbott et al., 2018b). Any tephra shard concentration peak that co-occurs with an increased level of IRD is not further discussed (see 2.2.2.). This includes the high tephra shard concentrations in the coarser-grained size fractions observed during GS-9 (Fig. 2e—f). In addition, depth-interval 4 stratigraphically correlates to several closely spaced tephra deposits recorded in the Greenland ice cores (Bourne et al., 2013, 2015) (Fig. 2b). Within this depth-interval, the smallest size fraction (i.e. 25-80 μm) is characterized by high shard concentrations including two distinct and multiple smaller peaks (Fig. 2d). Due to the complexity of this ash zone (see 2.1.1.) and the observed period of coeval IRD during GS-9, only the two distinct horizons are further investigated. The youngest tephra peak in this interval (i.e. at 3038—3039 cm) (Fig. 2d) falls extremely close to the previously identified tephra horizon presented by Sadatzki et al. (2019) (i.e. at 3040—3041 cm) (see 2.1.2.) and represents in all likelihood the same horizon. However, as there is a striking difference in shard concentration (i.e. >22 000 shards/g dry sediment for 3038—3039 cm versus >12 000 shards/g dry sediment for 3040—3041 cm) this more distinct tephra peak, only recorded in this high-resolution investigation, is further investigated in order to refine this horizon's stratigraphic position.

This study focuses on the following six layers, labeled as follows: Horizon A (2109—2110 cm), Horizon B (2134—2135 cm), Horizon C (2322—2323 cm), Horizon D (2648—2649 cm), Horizon E (3038-3039 cm) and Horizon F (3173—3174 cm) (Fig. 2). For each of these

horizons a comprehensive multiple grain geochemical analysis is executed and compared to the geochemical data of the Greenland ice core tephra deposits within broad stratigraphic windows.

3.2. Identified tephra horizons

3.2.1. Horizon A (2109—2110 cm)

Horizon A, stratigraphically deposited during GI-5 at 2109—2110 cm core depth, represents a rapid increase in shard concentration with a peak in the 25—80 μm fraction (Figs. 2d and 3c). To better visualize the shard profiles, the different concentrations of this layer are plotted versus depth (Fig. 3a—c). In particular, the profile of the fine-grained shards shows a sharp transition/flat bottom profile and, compared to the background shard concentrations of this particular depth-interval, a distinct tephra peak with a high concentration of >3100 shards/g dry sediment (Fig. 3c; Table 2). However, this peak is not mirrored in the coarser-grained shard profiles with only 2 and 6 shards/g dry sediment recorded in the >125 μm and 80—125 μm size fractions, respectively (Fig. 3a—b; Table 2).

The geochemical composition of Horizon A is homogeneous tholeiitic basalt (Fig. 3e). The major element composition shows a geochemical signature characterized by ranges of 50.08—51.08 wt. % SiO_2, 4.54—5.39 wt. % MgO, 0.41—0.61 wt. % K_2O and 3.10—3.53 wt. % TiO_2 (Fig. 3e—i). Overall, this compositional signature has a geochemical affinity with Kverkfjöll sourced material (Fig. 3f and i).

Three different deposits from the Greenland ice core tephra framework stratigraphically fit with Horizon A (Fig. 2b; Table 1). Of these, NGRIP 1950.50 m/NEEM 1689.25 m (GI-5) exhibits a tight and homogeneous Kverkfjöll composition, whereas the other two deposits consist of Katla type material (Fig. 3g). Prior to GS-6, another Kverkfjöll sourced deposit (i.e. NGRIP 1973.16 m/NEEM 1702.45 m (GI-6)) was identified by Bourne et al. (2015) (Figs. 2b and 3g; Table 1). A comparative analysis of Horizon A and those four ice core deposits, both visually (Fig. 3e—i) and statistically (Table 3), indicates that Horizon A is geochemically most similar to NGRIP 1950.50 m/NEEM 1689.25 m (GI-5) (SC = 0.98; D^2 = 0.93). However, as NGRIP 1973.16 m/NEEM 1702.45 m (GI-6) also consists of Kverkfjöll sourced material, Horizon A does also show some similarities to it (SC = 0.97; D^2 = 8.40) (Fig. 3g; Table 3). Nonetheless, the Al_2O_3 and TiO_2 concentrations clearly allow for the discrimination of NGRIP 1950.50 m/NEEM 1689.25 m (GI-5) from NGRIP 1973.16 m/NEEM 1702.45 m (GI-6) (Fig. 3i).

In summary, the shard profile of Horizon A is defined by a distinct and relatively high tephra concentration peak not co-occurring with increased IRD and consisting of a homogeneous geochemistry. These combined characteristics are defined as a deposit type-2A (Abbott et al., 2018b) arguing for Horizon A to be most likely deposited isochronously, via primary air fall. In addition, the clear visual, statistical and stratigraphical match provides independent evidence for a correlation between Horizon A and NGRIP 1950.50 m/NEEM 1689.25 m (GI-5). The identification of this isochron (i.e. MD99-2284_2109.5 cm) allows that this marine sediment core depth is used as a time-parallel marker for the following synchronization exercise (see 4.). The correlation to the Greenland tephra allows an age of 32.463 ka b2k from the GICC05 time-scale to be ascribed to this marine sediment core depth (Table 3).

3.2.2. Horizon B (2134—2135 cm)

Within the first depth-interval (2108—2148 cm), a second shard concentration peak in the 25—80 μm fraction (Horizon B) is observed at 2134—2135 cm core depth during, stratigraphically, late GS-6 (Figs. 2d and 4c). The shard profile of this layer is, compared to
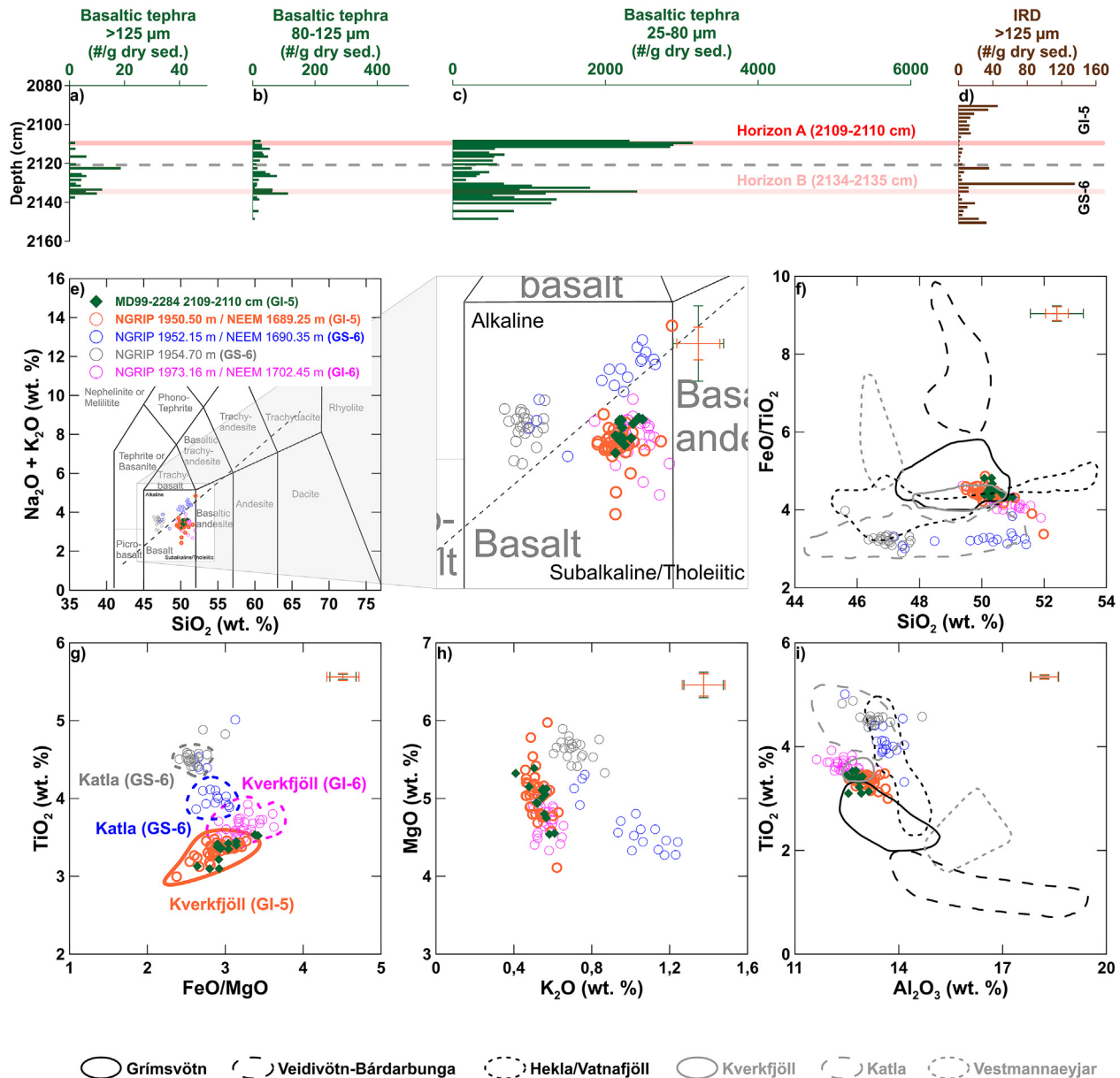
Fig. 3. Summary of Horizon A (2109−2110 cm). a-c) Tephrostratigraphy for selected depth-interval 1 (2108−2148 cm) with basaltic tephra shard concentrations for the different size fractions. Note: high-resolution areas are visible when there is no space left between the green bars. d) IRD concentrations. e-i) Comparison between the major elements of Horizon A (green diamonds) and stratigraphically fitting Greenland ice core horizons from GI-5, GS-6 and GI-6 (open circles) (Bourne et al., 2015). All data are normalized to an anhydrous basis (i.e. 100% total oxides). Error bars represent 2 standard deviations of replicate analyses of the BCR2g reference glass. e) Total alkalis vs. silica diagram (Le Bas et al., 1986). The dashed line indicates the boundary between the alkaline and subalkaline/tholeiitic series (MacDonald and Katsura, 1964). f) SiO_2 vs. FeO/TiO_2 biplot. g) FeO/MgO vs. TiO_2 biplot. h) K_2O vs. MgO biplot. i) Al_2O_3 vs. TiO_2 biplot. The different geochemical fields for Icelandic source volcanoes are based on glass analyses shown in Abbott et al. (2018a) and references within (here presented in plots f and i) and shown in Bourne et al. (2015) (here presented in plot g). (For interpretation of the references to color in this figure legend, the reader is referred to the Web version of this article.)

Table 2
Summary of tephra horizons detected in MD99-2284 between ca. 32 and 40 ka b2k. For each horizon, the following information is provided: label (including depth), shard concentration per counted size fraction, climatic event based on the age model presented in Sadatzki et al. (2019), deposit type based on the classification scheme presented in Abbott et al. (2018b), geochemistry after Le Bas et al. (1986) (TB = Tholeiitic Basalt, TAB = Transitional Alkali Basalt, R = Rhyolite) and most likely volcanic source.

MD99-2284 Tephra horizon	Tephra shard concentration (#/g dry sed.)			Climatic event	Deposit type	Geochemistry	Volcanic source
	>125 μm	80−125 μm	25−80 μm				
Horizon A (2109−2110 cm)	2	6	3 141	GI-5	type-2A*	TB	Kverkfjöll
Horizon B (2134−2135 cm)	6	62	2 414	GS-6	type-2B/2A*	TAB	Katla/Kverkfjöll
Horizon C (2322−2323 cm)	10	331	10 535	GI-6	type-2A	TB	Kverkfjöll
Horizon D (2648−2649 cm)	6	18	3 037	GI-7	type-2A	R	Katla
Horizon E (3038-3039 cm)	14	311	22 123	GI-8	type-2A	TB	Grímsvötn
Horizon F (3173−3174 cm)	45	730	6 911	GS-9	type-2B	TAB	Mixed

Table 3
Summary of the statistical comparisons between the detected tephra horizons in MD99-2284 and those from stratigraphically corresponding tephra horizons within the Greenland ice core tephra framework (Bourne et al., 2013, 2015). For each tephra horizon, the following information is provided: label (including depth and number of analysed shards (n)), stratigraphically corresponding ice core tephra horizons, their climatic event and age (Bourne et al., 2013, 2015) as well as the statistical parameters (SC = similarity coefficient (Borchardt et al., 1972; Hunt et al., 1995) and D^2 = statistical distance (Perkins et al., 1995, 1998) indicative of a geochemical fit. For statistical distance comparison, a critical value of 23.21 (10 degrees of freedom, 99% confidence interval) was used. The grey highlighted rows indicate the isochrons established in this study that can be used as time-parallel markers for synchronization (see 4.). Note: ^data is not included in the calculation of the statistical parameters.

MD99-2284 Tephra horizon	Greenland ice core Tephra horizon			Climatic event	NGRIP age (ka b2k)	Statistical comparison	
	GRIP	NEEM	NGRIP			SC	D^2
Horizon A **(2109-2110 cm)** **(n=14)**	**-**	**1689.25 m**	**1950.50 m**	**GI-5**	**32.463**	**0.98**	**0.93**
	-	*1690.35 m*	*1952.15 m*	*GS-6*	*32.522*	*0.92*	*27.70*
	-	-	*1954.70 m*	*GS-6*	*32.690*	*0.91*	*99.92*
	-	1702.45 m	1973.16 m	GI-6	33.686	0.97	8.40
						Total Pop. 1 / Pop. 2	Total Pop. 1 / Pop. 2
(2129-2130 cm) **Pop. 1** / Pop. 2 **56%** / 44% **(n=16)**	-	*1689.25 m*	*1950.50 m*	*GI-5*	*32.463*	*0.94* *0.92 / 0.95*	*8.23* *30.61 / 7.25*
	-	**1690.35 m**	**1952.15 m**	**GS-6**	**32.522**	**0.97** **0.97** / *0.94*	**2.85** **1.22** / *21.23*
	-	-	*1954.70 m*	*GS-6*	*32.690*	*0.91* *0.91 / 0.89*	*22.19* *21.03 / 93.71*
	-	1702.45 m	1973.16 m	GI-6	33.686	0.95 *0.93 / 0.97*	9.38 *32.06 / 6.16*
Horizon B **(2134-2135 cm)** **Pop.1** / Pop. 2 **63%** / 37% **(n=16)**	-	*1689.25 m*	*1950.50 m*	*GI-5*	*32.463*	*0.93* *0.91 / 0.96*	*9.45* *4.76 / 4.76*
	-	**1690.35 m**	**1952.15 m**	**GS-6**	**32.522**	**0.97** **0.97** / *0.93*	**1.95** **1.69** / *20.70*
	-	-	*1954.70 m*	*GS-6*	*32.690*	*0.91* *0.90 / 0.91*	*20.28* *28.80 / 61.30*
	-	1702.45 m	1973.16 m	GI-6	33.686	0.95 *0.92 / 0.99*	10.25 *49.26 / 2.94*
(2139-2140 cm) **Pop.1** / Pop.2 **56%** / 44% **(n=16)**	-	*1689.25 m*	*1950.50 m*	*GI-5*	*32.463*	*0.93* *0.91 / 0.94*	*12.47* *10.53 / 10.53*
	-	**1690.35 m**	**1952.15 m**	**GS-6**	**32.522**	0.96 **0.97** / *0.94*	2.51 **1.43** / *25.50*
	-	-	*1954.70 m*	*GS-6*	*32.690*	*0.91* *0.90 / 0.90*	*25.93* *36.58 / 49.22*
	-	1702.45 m	1973.16 m	GI-6	33.686	0.95 *0.92 / 0.98*	8.83 *49.86 / 4.21*
(2144-2145 cm) **Pop.1** / Pop. 2 **44%** / 56% **(n=16)**	-	1689.25 m	1950.50 m	GI-5	32.463	0.95 *0.93 / 0.97*	3.00 *2.22 / 2.2*
	-	**1690.35 m**	**1952.15 m**	**GS-6**	**32.522**	0.96 **0.97** / *0.93*	4.89 **1.66** / *22.65*
	-	-	*1954.70 m*	*GS-6*	*32.690*	*0.93* *0.93 / 0.91*	*12.15* *10.92 / 65.09*
	-	1702.45 m	1973.16 m	GI-6	33.686	0.95 *0.92 / 0.97*	5.66 *29.34 / 6.50*
Horizon C **(2322-2323 cm)** **(n=13)**	-	*1689.25 m*	*1950.50 m*	*GI-5*	*32.463*	*0.94*	*5.69*
	-	*1690.35 m*	*1952.15 m*	*GS-6*	*32.522*	*0.93*	*19.82*
	-	-	*1954.70 m*	*GS-6*	*32.690*	*0.89*	*51.21*
	-	**1702.45 m**	**1973.16 m**	**GI-6**	**33.686**	**0.97**	**1.78**
Horizon D **(2648-2649 cm)** **(n=10)**	-	-	*2009.15 m*	*GI-7*	*35.470*	*0.85*	*15.25*
Horizon E **(3038-3039 cm)** **(n=19)**	2195.45 m^	1755.60 m^	2064.35 m	GI-8	38.041	0.96	14.57
	-	-	2065.65 m	GI-8	38.081	0.95	14.62
	-	-	2065.80 m	GI-8	38.086	0.95	21.64
	2197.45 m^	1757.10 m^	2066.95 m	GI-8	38.121	0.95	*32.60*
	2195.45 m - **2197.45 m^**	**1755.60 m -** **1757.10 m^**	**2064.35 m -** **2066.95 m**	**GI-8**	**38.041 -** **38.121**	**0.96**	**15.85**
	2201.50 m - *2207.00 m^*	*1759.85 m −* *1764.25 m^*	*2071.50 m −* *2079.40 m*	*GS-9*	*38.309 −* *38.826*	*0.89*	*41.83*
	-	-	*2085.80 m*	*GS-9*	*39.258*	*0.91*	*79.80*

Horizon F (3173-3174 cm) Population **1** **(n= 5)** (>125 μm: n=4) (80-125 μm: n=1) (25-80 μm: n=0)	2195.45 m – 2197.45 m^	1755.60 m - 1757.10 m^	2064.35 m - 2066.95 m	GI-8	38.041 – 38.121	0.89	584.94
	2201.50 m - 2207.00 m^	1759.85 m – 1764.25 m^	2071.50 m – 2079.40 m	GS-9	38.309 – 38.826	0.83	464.60
	2213.05 m^	-	2085.80 m	GS-9	39.258	0.94	27.99
	-	-	2100.65 m	GS-10	40.218	0.85	150.67
	2227.15 m^	1780.20 m^	2101.55 m – 2103.98 m	GS-10	40.275 – 40.428	0.88	589.81
Horizon F (3173-3174 cm) Population **2** **(n=31)** (>125 μm: n=2) (80-125 μm: n=12) (25-80 μm: n=17)	2195.45 m – 2197.45 m^	1755.60 m - 1757.10 m^	2064.35 m - 2066.95 m	GI-8	38.041 – 38.121	0.86	196.08
	2201.50 m - 2207.00 m^	1759.85 m – 1764.25 m^	2071.50 m – 2079.40 m	GS-9	38.309 – 38.826	0.81	204.76
	2213.05 m^	-	2085.80 m	GS-9	39.258	0.93	20.02
	-	-	2100.65 m	GS-10	40.218	0.83	104.70
	2227.15 m^	1780.20 m^	2101.55 m – 2103.98 m	GS-10	40.275 – 40.428	0.86	184.36
Horizon F (3173-3174 cm) Population **3** **(n=23)** (>125 μm: n=2) (80-125 μm: n=4) (25-80 μm: n=17)	2195.45 m – 2197.45 m^	1755.60 m - 1757.10 m^	2064.35 m - 2066.95 m	GI-8	38.041 – 38.121	0.94	15.40
	2201.50 m - 2207.00 m^	1759.85 m – 1764.25 m^	2071.50 m – 2079.40 m	GS-9	38.309 – 38.826	0.88	39.76
	2213.05 m ^	-	2085.80 m	GS-9	39.258	0.93	58.19
	-	-	2100.65 m	GS-10	40.218	0.90	15.22
	2227.15 m^	1780.20 m^	2101.55 m – 2103.98 m	GS-10	40.275 – 40.428	0.93	14.69
Horizon F (3173-3174 cm) Population **4** **(n=30)** (>125 μm: n=1) (80-125 μm: n=8) (25-80 μm: n=21)	2195.45 m – 2197.45 m^	1755.60 m - 1757.10 m^	2064.35 m - 2066.95 m	GI-8	38.041 – 38.121	0.88	25.38
	2201.50 m - 2207.00 m^	1759.85 m – 1764.25 m^	2071.50 m – 2079.40 m	GS-9	38.309 – 38.826	0.84	39.05
	2213.05 m^	-	2085.80 m	GS-9	39.258	0.88	38.58
	-	-	2100.65 m	GS-10	40.218	0.86	20.95
	2227.15 m^	1780.20 m^	2101.55 m – 2103.98 m	GS-10	40.275 – 40.428	0.87	24.57

Horizon A, less characteristic of a single primary tephra-fall event (Figs. 3c and 4c). Therefore, in addition to the concentration peak, the geochemistry of three additional depths within this shard profile (i.e. one depth located 5 cm above the peak and two depths located 5 and 10 cm below the peak) were analysed and visualized (Fig. 4e−k). Within this study, the peak depth (i.e. 2134-2135 cm) is labeled as Horizon B whereas the additional geochemical data within this shard profile are referred to by their respective core depths.

Horizon B has, within the fine-grained shard profile, a peak concentration of >2400 shards/g dry sediment with a tail in both directions (i.e. a gradational upward span of 5 cm and 10 cm downwards) (Fig. 4c and e; Table 2). The >125 μm and 80−125 μm size fractions show concentrations of 6 and 62 shards/g dry sediment, respectively, but, compared to the fine-grained shard profile, do not record the gradational up- and downward spread (Fig. 4a−b; Table 2). Importantly, the IRD record shows, despite an exception 4 cm above the tephra concentration peak, generally low values for this interval and thus, no co-occurring IRD increase with Horizon B (Fig. 4d).

The major element analyses from Horizon B exhibit a bimodal composition predominantly consisting of alkaline basalt and to a lesser extent tholeiitic basalt (Fig. 4g; dark green labeled as MD99-2284 2134−2135 cm). These two geochemical populations show a clear difference in their oxide concentrations (Fig. 4g−k; dark green diamonds versus triangles). The dominant population of Horizon B (i.e. population 1) records SiO_2 concentrations of 48.07−52.22 wt. %, MgO concentrations of 4.34−5.36 wt. %, K_2O concentrations of 0.87−1.23 wt. % and TiO_2 concentrations of 3.83−4.33 wt. % (Fig. 4g−k: dark green diamonds), whereas the minor population

(i.e. population 2) is characterized by 49.36−51.18 wt. % SiO_2, 4.69−4.99 wt. % MgO, 0.51−0.59 wt. % K_2O and 3.28−3.92 wt. % TiO_2 (Fig. 4g−k: dark green triangles). The shards grouped as populations 1 and 2 display affinities to Katla and Kverkfjöll sourced material, respectively (Fig. 4h and k: dark green diamonds and triangles).

The close stratigraphic relationship between Horizons A and B means that the same Greenland ice core horizons to which Horizon A was compared fall within the stratigraphical proximity of Horizon B (Fig. 2b; Table 1). These ice core layers show either a Kverkfjöll or a Katla sourced geochemical signature (Fig. 4i; Table 1). A comparative analysis between population 1 of Horizon B and those four ice core deposits, both visually (Fig. 4g−k; dark green diamonds) and statistically (Table 3), shows clearly that population 1 is geochemically most similar to NGRIP 1952.15 m/NEEM 1690.35 m (GS-6) (SC = 0.97; D^2 = 1.69). However, in the SiO_2 concentrations, a slight offset is observed between population 1 and NGRIP 1952.15 m/NEEM 1690.35 m (GS-6) (Fig. 4h). As the secondary standard analyses from the two analytical periods also show a consistent slight offset in SiO_2 (See Supplementary Data for all standard measurements), it is most likely that the offset for the samples are, at least partially, explained by this variation reported in the standard analyses. And thus, the latter is partly regarded as an analytical offset rather than a real one that would prevent the correlation of the two horizons. Furthermore, even though NGRIP 1954.70 m (GS-6) has a Katla sourced geochemical signature and stratigraphic similarities, there is no correlative link between this ice core layer and any of the single glass shard measurements from Horizon B (Fig. 4g−k; Table 3). The latter ice core layer exhibits a
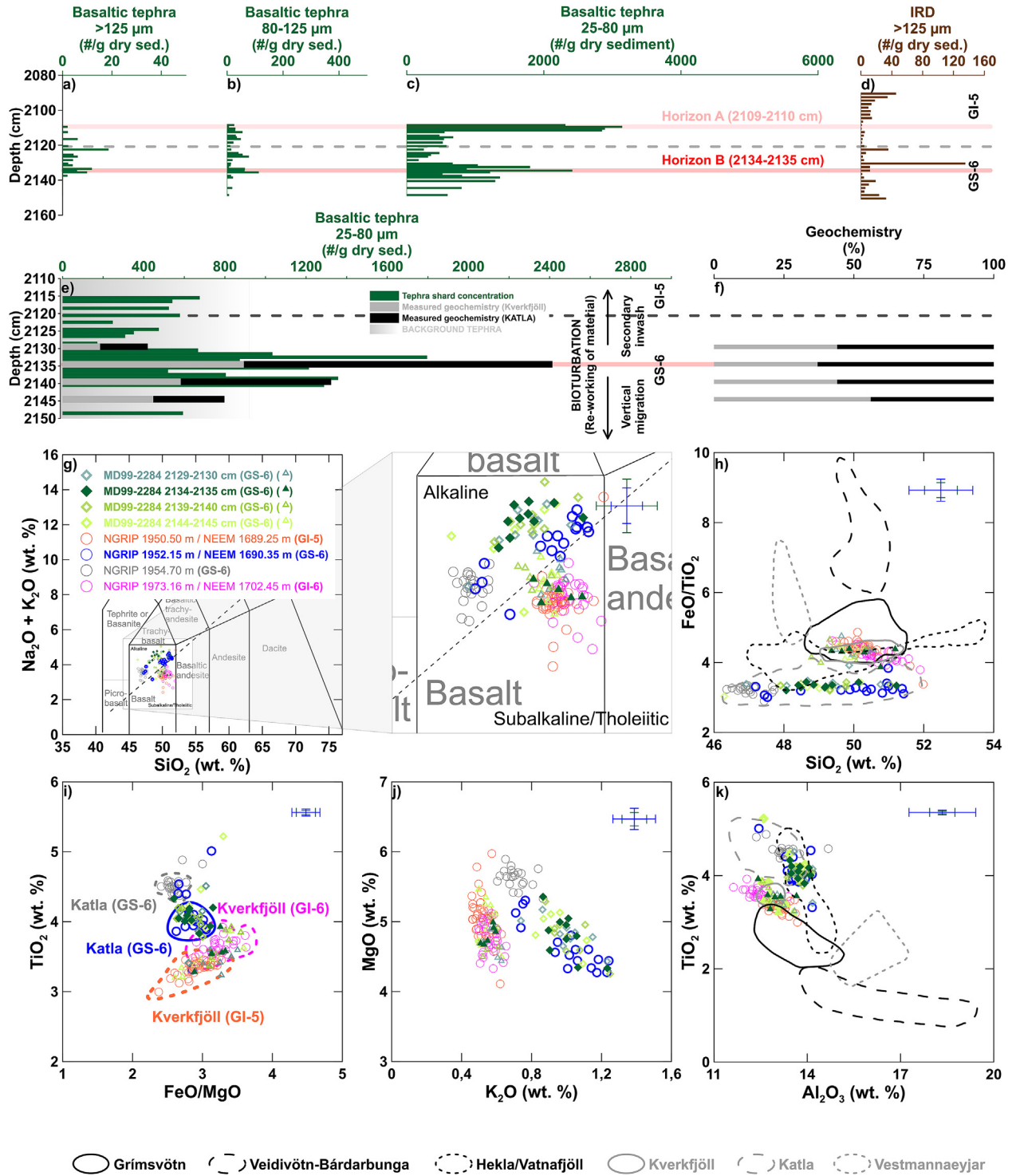
Fig. 4. Summary of Horizon B (2134−2135 cm). a-c) Tephrostratigraphy for selected depth-interval 1 (2108−2148 cm) with basaltic tephra shard concentrations for the different size fractions. Note: high-resolution areas are visible when there is no space left between the green bars. d) IRD concentrations. e) Cryptotephra shard profile including the relative distribution of population 1 (black) & 2 (grey) within peak and tails. f) Percentage of shards from population 1 (black) and 2 (grey) for the analysed samples versus depth. g-k) Comparison between the major elements of Horizon B (green) and stratigraphically fitting Greenland ice core horizons from GI-5, GS-6 and GI-6 (open circles) (Bourne et al., 2015). From each depth of the marine samples, the major and minor populations (i.e. population 1 (diamonds) versus population 2 (triangles)) are plotted separately. All data are normalized to an anhydrous basis (i.e. 100% total oxides). Error bars are representing 2 standard deviations of replicate analyses of the BCR2g reference glass. g) Total alkalis vs. silica diagram (Le Bas et al., 1986). The dashed line indicates the boundary between the alkaline and subalkaline/tholeiitic series (MacDonald and Katsura, 1964). h) SiO_2 vs. FeO/TiO_2 biplot. i) FeO/MgO vs. TiO_2 biplot. j) K_2O vs. MgO biplot. k) Al_2O_3 vs. TiO_2 biplot. The different geochemical fields for Icelandic source volcanoes are based on glass analyses shown in Abbott et al. (2018a) and references within (here presented in plots h and k) and shown in Bourne et al. (2015) (here presented in plot i). (For interpretation of the references to color in this figure legend, the reader is referred to the Web version of this article.)

tighter geochemical population with slightly higher TiO_2 and MgO, and somewhat lower SiO_2 concentrations compared to the full compositional range of Horizon B, which is also confirmed by the statistical parameters (Table 3). While population 1 (Fig. 4g−k: dark green diamonds) is stratigraphically, visually and statistically linked to NGRIP 1952.15 m/NEEM 1690.35 m (GS-6) and decoupled from NGRIP 1954.70 m (GS-6), population 2 of Horizon B (Fig. 4g−k: dark green triangles) shows some affinities, both visually and statistically (Table 3), to the Kverkfjöll sourced ice core horizons. Statistically, population 2 shows the strongest correlation (SC = 0.99; D^2 = 2.94) (Table 3) to the stratigraphically older horizon (i.e. NGRIP 1973.16 m/NEEM 1702.45 m (GI-6)).

As the profile of the fine-grained shards is characterized by a tail in both an up- and downward direction and the bimodal composition reflects a double population, Horizon B has characteristics akin to deposit type-2B (Abbott et al., 2018b). This deposit type suggests that Horizon B is potentially hampered in its ability to be correlated to individual ice core horizons and thus, requires some additional investigations (Abbott et al., 2018a, 2018b). A more comprehensive analysis of the geochemistry from the entire shard profile was executed in order to investigate if secondary transport and depositional processes compromised the isochronous integrity of this tephra horizon. The geochemistry was measured for one sample located 5 cm above and two samples 5 and 10 cm below Horizon B (Fig. 4g−k: 3 different lighter green colored labels compared to Horizon B). Akin to the geochemical signature of Horizon B, these additional samples also contain both Katla and Kverkjöll sourced material (Fig. 4g−k; Table 3). However, it is observed that Horizon B has proportionally more population 1 shards (Katla sourced) compared to the other samples (Fig. 4e−f; Table 3). These results argue for a certain degree of bioturbative reworking and/or secondary in wash upward as well as bioturbative reworking and/or vertical migration of shards downward of the peak concentration (Fig. 4e) (Davies, 2015; Griggs et al., 2015; Abbott et al., 2018b). These post-depositional processes, mixing a single depositional event with existing background tephra, explains the decreasing trend of the Katla-sourced shards away from Horizon B. Indeed, compared to the tight homogeneous Katla-sourced population 1, population 2, which shows a strong correlation to the stratigraphically older NGRIP 1973.16 m/NEEM 1702.45 m (GI-6) horizons (Fig. 4g−k; Table 3), exhibits a much wider geochemical range within the full compositional range of Kverkfjöll sourced material. This wider scatter of shards likely reflects some heterogeneity within the second population due to post-depositional processes. Despite the initial signs of a non-isochronous deposit, features such as no coeval IRD (Fig. 4d), a link with the existing ice core horizon in a similar stratigraphic position (Figs. 2 and 4; Table 3), and the relative dominance of population 1 within the shard profile (Fig. 4e−f) provides strong evidence to suggest that population 1 of Horizon B reflects an air fall deposition from a single volcanic eruption. However, population 1 of Horizon B was deposited in addition to a background signal (i.e. population 2) that shows strong characteristics of a secondary deposition and/or reworked material from another eruption. The clear stratigraphic, visual and statistical match between population 1 of Horizon B and NGRIP 1952.15 m/NEEM 1690.35 m (GS-6) confirms its potential use as a time-parallel marker for future synchronization (i.e. MD99-2284_2134.5 cm) (see 4.). This correlation allows us to ascribe a GICC05 age of 32.522 ka b2k to the marine sediment core depth (Table 3).

3.2.3. Horizon C (2322−2323 cm)

During GI-6, a clear peak in shard concentration (Horizon C) is observed at 2322−2323 cm core depth (Figs. 2d and 5a-c). Horizon C shows a similar shard profile between the 25−80 μm and 80−125 μm size fractions with concentrations of >10 500 and >300 shards/g dry sediment, respectively (Fig. 5b−c; Table 2). Within both grain-sizes, the shard profile shows a high and distinct tephra peak with up- and downward tails of approximately 5 cm in both directions. However, the >125 μm size fraction has a slightly different profile with a concentration peak of 10 shards/g dry sediment 2 cm below the peaks in the smaller size fractions (Fig. 5a; Table 2). Different settling velocities through the ocean and/or heavier material moving through soft sediment might explain such a depth-offset (Enache and Cumming, 2006).

Horizon C is characterized by a homogeneous tholeiitic basaltic composition with major elements between 49.75 and 51.28 wt. % SiO_2, 3.98−5.02 wt. % MgO, 0.52−0.63 wt. % K_2O and 3.1−3.8 wt. % TiO_2 with the exception of two outliers (Fig. 5e−i). This geochemical signature shows a strong affinity to Kverkfjöll sourced volcanic material (Fig. 5f and i).

Only one tephra deposit preserved in the Greenland ice core framework correlates, stratigraphically, to Horizon C (Fig. 2b; Table 1). This ice core deposit (i.e. NGRIP 1973.16 m/NEEM 1702.45 m (GI-6)) has a homogeneous Kverkfjöll geochemical composition (Fig. 5g). However, the ice core deposit of GI-5 (i.e. NGRIP, 1950.50 m/NEEM 1689.25 m) also has a similar Kverkfjöll sourced geochemistry (Fig. 5g). Therefore, Horizon C was compared, both visually (Fig. 5e−i) and statistically (Table 3), to both ice core deposits. These results suggest that Horizon C has a better match with the glass composition of NGRIP 1973.16 m/NEEM 1702.45 m (GI-6) (SC = 0.97; D^2 = 1.78) (Fig. 5g; Table 3).

The pronounced peaks in shard concentration are distinct across all grain-size fractions, with a slight depth-offset noted for the highest size fraction. Horizon C is characterized by a clear peak in shard concentration not associated with IRD input and a homogeneous geochemical population, which argues for a single depositional event that is most likely dominated by a primary air fall deposition. This allows Horizon C to be defined as a deposit type-2A (Abbott et al., 2018b). Combining this attribution with the clear statistical, visual and stratigraphical fit, Horizon C can be considered isochronous and is correlated to NGRIP 1973.16 m/NEEM 1702.45 m (GI-6). Due to the pronounced tephra peak within the 25−80 μm size fraction and the mechanisms that could have influenced the stratigraphic position of the heavier shards, the isochron is labeled as MD99-2284_2322.5 cm and used as a time-parallel marker for future synchronization (see 4.). Due to the correlation with NGRIP 1973.16 m/NEEM 1702.45 m (GI-6), an age of 33.686 ka b2k on the GICC05 time-scale is ascribed to the marine sediment core depth (Table 3).

3.2.4. Horizon D (2648−2649 cm)

Horizon D is recorded at a core depth of 2648−2649 cm, stratigraphically deposited during GI-7 and defined as a clearly distinct concentration peak in the fine-grained size fraction (Figs. 2d and 6c). A high concentration of >3000 shards/g dry sediment is recorded within the 25−80 μm size fraction (Fig. 6c; Table 2). However, in the coarser-grained fractions this deposit is not well-pronounced with tephra concentrations of 6 and 18 shards/g dry sediment in the >125 μm and 80−125 μm size fractions, respectively (Fig. 6a−b; Table 2).

The geochemical composition of glass shards from the deposit displays a tight homogeneous rhyolitic population with the exception of two outliers (Fig. 6e). The major elements are characterized by ranges of 71.22−73.84 wt. % SiO_2, 3.38−4.02 wt. % FeO, 3.61−3.90 wt. % K_2O and 0.85−1.57 wt. % CaO (Fig. 6e−i). Although theses values are typical for rhyolitic tephras from Iceland, this compositional signature shows the strongest affinity to Katla
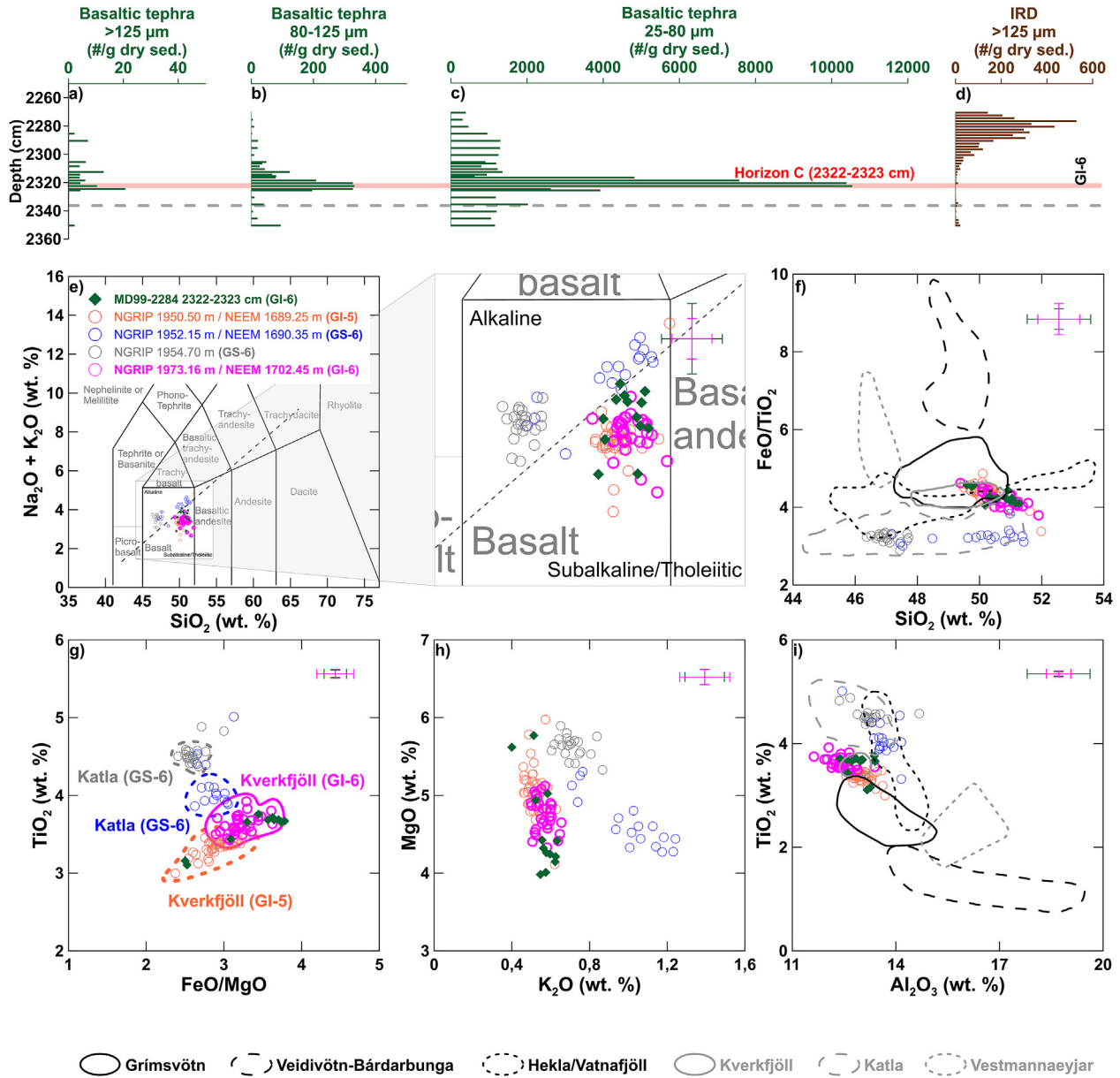
Fig. 5. Summary of Horizon C (2322−2323 cm). a-c) Tephrostratigraphy for selected depth-interval 2 (2270−2350 cm) with basaltic tephra shard concentrations for the different size fractions. Note: high-resolution areas are visible when there is no space left between the green bars. d) IRD concentrations. e-i) Comparison between the major elements of Horizon C (green diamonds) and stratigraphically fitting Greenland ice core horizons from GI-5, GS-6 and GI-6 (open circles) (Bourne et al., 2015). All data are normalized to an anhydrous basis (i.e. 100% total oxides). Error bars are representing 2 standard deviations of replicate analyses of the BCR2g reference glass. e) Total alkalis vs. silica diagram (Le Bas et al., 1986). The dashed line indicates the boundary between the alkaline and subalkaline/tholeiitic series (MacDonald and Katsura, 1964). f) SiO_2 vs. FeO/TiO_2 biplot. g) FeO/MgO vs. TiO_2 biplot. h) K_2O vs. MgO biplot. i) Al_2O_3 vs. TiO_2 biplot. The different geochemical fields for Icelandic source volcanoes are based on glass analyses shown in Abbott et al. (2018a) and references within (here presented in plots f and i) and shown in Bourne et al. (2015) (here presented in plot g). (For interpretation of the references to color in this figure legend, the reader is referred to the Web version of this article.)

sourced volcanic material (Fig. 6f, g and 6i). Notably, the rather high FeO concentrations allow for a discrimination between the different geochemical fields and indicate how this geochemistry overlaps with published data of the Vedde Ash (Fig. 6h).

From a stratigraphic point of view, one ice core tephra deposit falls within the proximity of Horizon D (Fig. 2b; Table 1). However, this deposit (i.e. NGRIP 2009.15 m (GI-7)) exhibits a heterogeneous dacite to rhyolite composition (Fig. 6e−i). It is clear from the bivariate plots (Fig. 6e−i), and statistically confirmed (Table 3), that Horizon D does not correlate to this ice core tephra deposit (SC = 0.85; D^2 = 15.25). In addition, the geochemistry of Horizon D does not correspond to any other tephra horizons with a similar

stratigraphic position in either ice core or marine records.

Based on the distinct concentration peak, the homogeneity of the geochemical composition and no coeval IRD, Horizon D is classified as a deposit type-2A (Abbott et al., 2018b) showing all evidence of a primary air fall deposit with a clear isochronous nature. However, as there is no correlation with the known Greenland ice core tephra framework, Horizon D cannot be used as a time-parallel marker in this work. Nevertheless, it does offer the potential to be used for future correlations if it can be traced in other climate archives.
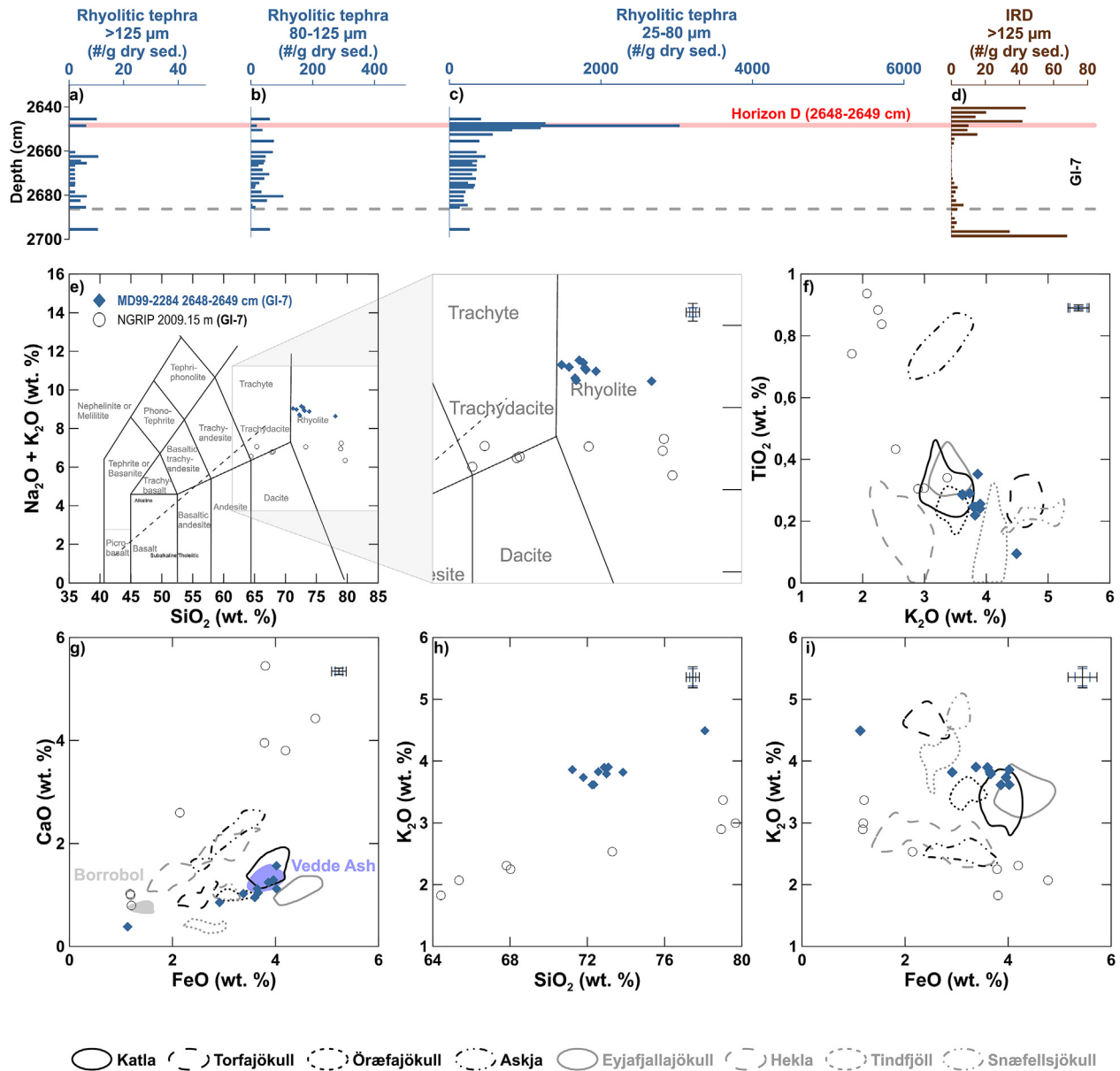
Fig. 6. Summary of Horizon D (2648−2649 cm). a-c) Tephrostratigraphy for selected depth-interval 3 (2645−2700 cm) with rhyolitic tephra shard concentrations for the different size fractions. Note: high-resolution areas are visible when there is no space left between the blue bars. d) IRD concentrations. e-i) Comparison between the major elements of Horizon D (blue diamonds) and stratigraphically fitting Greenland ice horizons from GI-7 (open circles) (Bourne et al., 2015). All data are normalized to an anhydrous basis (i.e. 100% total oxides). Error bars are representing 2 standard deviations of replicate analyses of the Lipari Obsidian reference glass. e) Total alkalis vs. silica diagram (Le Bas et al., 1986). The dashed line indicates the boundary between the alkaline and subalkaline/tholeiitic series (MacDonald and Katsura, 1964). f) K_2O vs. TiO_2 biplot. g) FeO vs. CaO biplot. h) SiO_2 vs. K_2O biplot. i) FeO vs. K_2O biplot. The different geochemical fields for Icelandic source volcanoes are based on glass analyses shown in Jennings et al. (2014) and references within (here presented in plots f, g and i). The geochemical envelopes for Borrobol and Vedde Ash are taken from Koren et al. (2008) (here presented in plot g). (For interpretation of the references to color in this figure legend, the reader is referred to the Web version of this article.)

3.2.5. Horizon E (3038-3039 cm)

Within the final depth-interval selected in this study, an extremely high and distinct tephra peak with concentrations of >22 000 shards/g dry sediment is observed in the 25−80 μm size fraction at 3038−3039 cm core depth (Figs. 2d and 7c; Table 2). This tephra layer is labeled Horizon E and stratigraphically deposited during GI-8. Within the high-resolution profile, the peak clearly stands out with no signs of a gradational tail. However, only 14 and >300 shards/g dry sediment are recorded within the >125 μm and 80−125 μm size fractions, respectively (Fig. 7a−b; Table 2). Compared to the glass shard concentrations down-core, these numbers do not stand out and thus, the coarser-grained shard

profiles do not capture this tephra layer within the marine sediment core (Fig. 7a−b).

Horizon E has a tholeiitic basaltic composition with the exception of one outlier (Fig. 7e). The rather tight ranges in its major elements, with values of 48.69−50.32 wt. % SiO_2, 4.92−5.92 wt. % MgO, 0.39−0.56 wt. % K_2O and 2.94−3.26 wt. % TiO_2, reflect a strong homogeneity (Fig. 7e−i) and a strong affinity with the Grímsvötn volcanic region (Fig. 7f and i).

GI-8 is well-known for the widely dispersed FMAZ III deposit in the marine realm (e.g. Rasmussen et al., 2003; Wastegård et al., 2006) and the series of eruptions recorded in the Greenland ice cores (Bourne et al., 2013, 2015). Stratigraphically, Horizon E
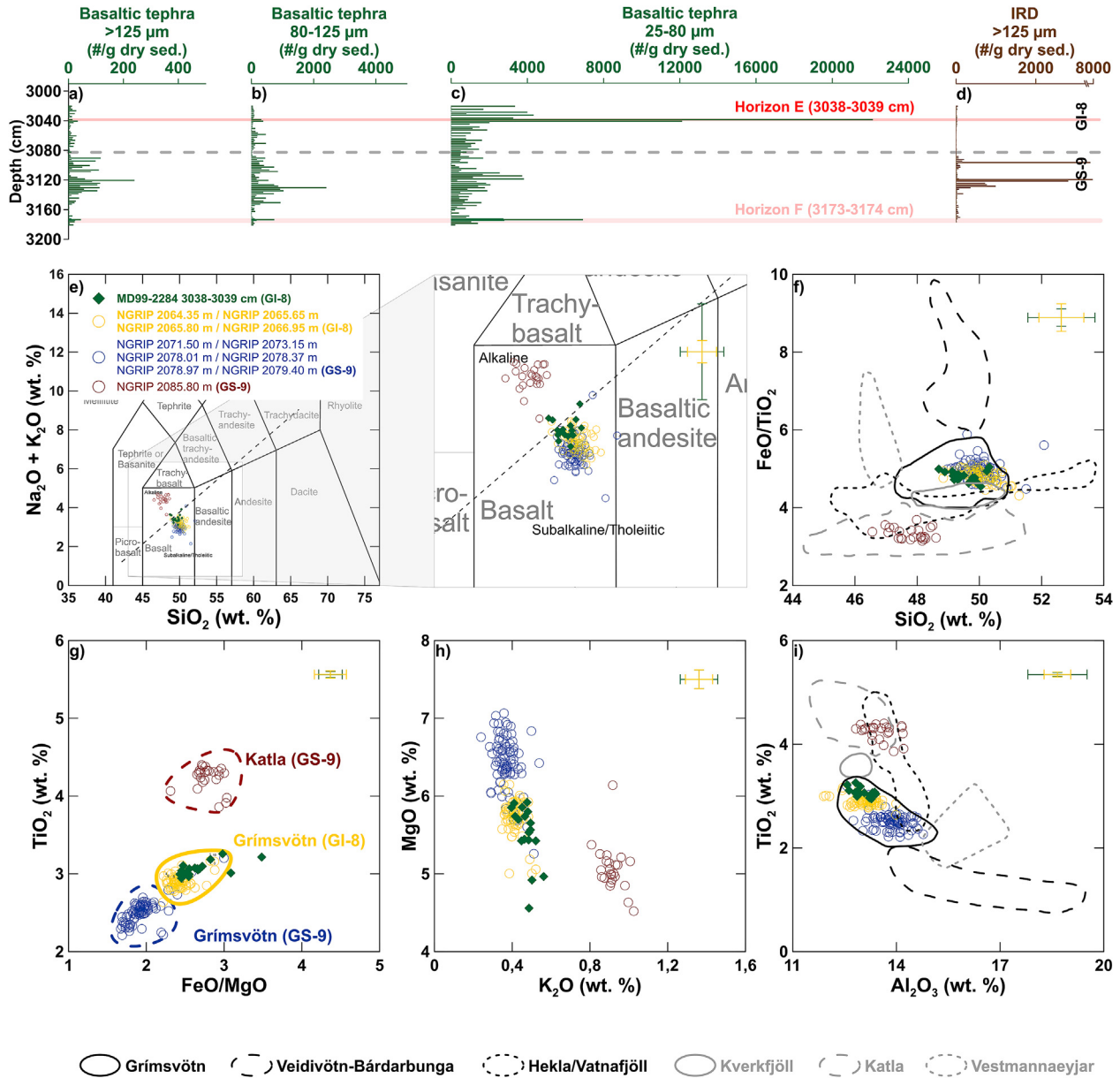
Fig. 7. Summary of Horizon E (3038-3039 cm). a-c) Tephrostratigraphy for selected depth-interval 4 (3020−3180 cm) with basaltic tephra shard concentrations for the different size fractions. Note: high-resolution areas are visible when there is no space left between the green bars. d) IRD concentrations. e-i) Comparison between the major elements of Horizon E (green diamonds) and stratigraphically fitting Greenland ice core horizons (NGRIP) from GI-8 and GS-9 (open circles) (Bourne et al., 2013). All data are normalized to an anhydrous basis (i.e. 100% total oxides). Error bars are representing 2 standard deviations of replicate analyses of the BCR2g reference glass. e) Total alkalis vs. silica diagram (Le Bas et al., 1986). The dashed line indicates the boundary between the alkaline and subalkaline/tholeiitic series (MacDonald and Katsura, 1964). f) SiO_2 vs. FeO/TiO_2 biplot. g) FeO/MgO vs. TiO_2 biplot. h) K_2O vs. MgO biplot. i) Al_2O_3 vs. TiO_2 biplot. The different geochemical fields for Icelandic source volcanoes are based on glass analyses shown in Abbott et al. (2018a) and references within (here presented in plots f and i) and shown in Bourne et al. (2015) (here presented in plot g). (For interpretation of the references to color in this figure legend, the reader is referred to the Web version of this article.)

corresponds to several tephra deposits (Fig. 2b; Table 1). With the exception of NGRIP 2085.80 m (GS-9), consisting of Katla sourced volcanic material, all of these ice core deposits exhibit geochemical homogeneity and Grímsvötn-like compositions (Fig. 7g; Table 1). However, based on their TiO_2 content, the tephra deposits from GI-8 (Fig. 7g−i; yellow) can be discriminated from those deposited during GS-9 (Fig. 7g−i; blue). A visual (Fig. 7e−i) and statistical (Table 3) comparison of Horizon E and the GI-8/GS-9 ice core deposits shows that, despite the fact that the GS-9 ice core tephra layers are part of the wider Grímsvötn-sourced geochemical envelope, they do not correlate to Horizon E, neither visually (Fig. 7e−i; blue) nor statistically (Table 3). Contrary, the comparison

highlights strong similarities between Horizon E and the, stratigraphically consistent, GI-8 ice core tephra layers (Fig. 7e−i; yellow). Nonetheless, defining a correlation between Horizon E and an individual GI-8 ice core horizon is very difficult. In particular, when eliminating any offset data point (i.e. non-Grimsvötn sourced data points in Fig. 7e−i) consistently for each ice core horizon, none of those four GI-8 horizons correlate separately to Horizon E with a SC >0.97 (Table 3). Therefore, it is not possible to disentangle the four separate GI-8 ice core horizons.

The distinct concentration peak within the 25−80 μm fraction shows strong evidence for a single depositional event. Additionally, the geochemical homogeneity and lack of IRD supports the

isochronous nature of Horizon E and thus, this horizon is categorized as a deposit type-2A (Abbott et al., 2018b). Due to its deposit type, the clear geochemical and stratigraphical match with the GI-8 NGRIP deposits, Horizon E is considered an independent time-parallel marker, labeled as MD99-2284_3038.5 cm. This isochron corresponds to the four GI-8 NGRIP horizons that were deposited within a time-span of 80 years (i.e. between 38.041 and 38.121 ka b2k) (Table 3). Hence, the average age of this time-interval (i.e. 38.081 ± 0.040 ka b2k on the GICC05 time-scale) is ascribed to this marine sediment core depth (Table 3). This finding refines the previously reported stratigraphic position of this tephra horizon (Sadatzki et al., 2019; see 2.1.2.). However, this refined stratigraphic position (i.e. 2 cm core upwards) does not affect any results or conclusions presented in that study. Nonetheless, the established isochron presented in this study is further used as a time-parallel marker for the synchronization exercise in this work (see 4.).

3.2.6. Horizon F (3173−3174 cm)

Horizon F, deposited during GS-9, represents a high and distinct shard concentration peak observed at 3173−3174 cm core depth in all size fractions including a small gradational up- and downward tail spanning ca. 5 cm (Figs. 2d and 8a-c). More specifically, concentrations of >6900, >700 and 45 shards/g dry sediment are observed for the 25−80 μm, 80−125 μm and >125 μm size fractions, respectively (Fig. 8a−c; Table 2). Horizon F is observed during a time-interval of low IRD input and thus, was most likely not deposited by icebergs (Fig. 8d). Compared to the previously described horizons, the coarser-grained size fractions show the highest concentration values within this study (Table 2). So, in contrast to the others horizons, single shard geochemical measurements were conducted on all size fractions (Fig. 8e−i).

The geochemistry of Horizon F has a particularly heterogeneous composition across all size fractions including shards with trachy-basaltic, alkaline basaltic, basaltic andesitic and tholeiitic compositions (Fig. 8e). Despite the wide heterogeneity, with major elements between 46.74 and 54.40 wt. % SiO_2, 2.76 and 6.08 wt. % MgO, 0.40 and 1.19 wt. % K_2O, and 2.18 and 4.83 wt. % TiO_2 (Fig. 8e−i), the analyses can be grouped into four distinct populations, present in all size fractions (population 1−4; Fig. 8e−i; Table 3). The different populations show affinities with Grímsvötn, Katla and other volcanic sources (Fig. 8f and i), which suggests that the horizon is an amalgamation of material sourced from multiple volcanic centers and thus, different volcanic eruptions.

Stratigraphically, Horizon F falls between the many different ice core layers deposited during GS-9 and GI-8, and three tephra deposits during GS-10 (Fig. 2b; Table 1). With the exception of NGRIP 2085.80 m (GS-9), consisting of Katla sourced volcanic material, all of these deposits are characterized by a Grímsvötn geochemistry (Fig. 8g) and, similar to Horizon E, they can be discriminated based on their TiO_2 content (Fig. 8g−i). However, no single Horizon F population correlates geochemically, neither visually (Fig. 8e−i) nor statistically (Table 3), to any of the different Grímsvötn sourced ice core deposits. Even though population 2 shows some affinities to Katla sourced material, a conclusive link with NGRIP 2085.80 m (GS-9) cannot be defined (Fig. 8e−i; Table 3).

Despite a clear concentration peak and no coeval IRD, Horizon F is also characterized by an up- and downward spanning and heterogeneous composition. This horizon possesses all the characteristics of a deposit type-2B (Abbott et al., 2018b). Secondary deposition mechanisms such as bottom current reworking and/or sea ice rafting most likely explain the recording of high and heterogeneous concentrations (Griggs et al., 2014). It might be possible that this mixture reflects an input of re-worked material picked up from the sill located south of the core location and along the

pathway of the Atlantic water inflow. In addition, it has been shown that during this time-period the core site might have been influenced by some seasonal sea ice melting (Sadatzki et al., 2019), which could have led to secondary deposition of tephra. A combination of these mechanisms potentially explains the observed mixture of geochemical populations. Overall, due to its non-isochronous characteristics, Horizon F cannot be used for any future synchronization or correlations.

4. Synchronization of disparate palaeo-records

In this study, the targeted cryptotephra investigation of MD99-2284 resulted in the identification of four isochrons within a time-span of ca. 8000 years that were assigned the GICC05 ages of their correlative NGRIP tephra horizons (Table 4; see 3.2.). These independent cryptotephra time-parallel markers, including the climatic information that can be derived from using them as tuning-points, are used to synchronize MD99-2284 to NGRIP (Fig. 9).

This synchronization is executed in different steps starting from the ARM/SST-tuning approach presented by Sadatzki et al. (2019) (Fig. 9a). The SST and ARM records (Dokken et al., 2013) used for the chronology of Sadatzki et al. (2019) (see 2.1.2.) are plotted on top of the NGRIP $\delta^{18}O$ record (Fig. 9). The latter is presented as a 25 point moving average in order to have a resolution more similar to the marine SST record. Additionally, the ARM/SST-based tuning-points (Fig. 9a−c; dark grey crosses) and the sedimentation-rates resulting from the chronology are visualized (Fig. 9).

Subsequently, the four new isochrons are added as tuning-points (Fig. 9b; colored crosses) to the existing age model (Sadatzki et al., 2019). This results in only a slightly modified version based on ARM/SST + Tephra isochron-tuning (Fig. 9b). However, the isochrons provide new and important information. In particular, by constraining the GS-6 to GI-5 transition with two independent cryptotephra time-parallel markers, the relationship between marine and atmospheric temperature (i.e. MD99-2284 SST and NGRIP $\delta^{18}O$) during this specific stadial-interstadial transition is resolved. Specifically, the independent isochrons (59 years apart) prior to and after the abrupt transition provide convincing evidence for a synchronous and abrupt increase of marine and atmospheric temperatures over this transition (Fig. 9b), consistent with the findings of earlier tephra-based ice-marine synchronizations for other transitions (e.g. Austin et al., 2004; Wastegård et al., 2006; Davies et al., 2008). Subsequently, it is further assumed that this pattern of a simultaneous increase in marine SST and ice core $\delta^{18}O$ from stadial into interstadial conditions occurs in a consistent manner for the other stadial-interstadial transitions within this study.

For each transition into an interstadial, we create new tuning-points (TP_{in}) by correlating the onset of the marine SST increase to the start of the ice core $\delta^{18}O$ increase (Fig. 9c; green crosses; Table 4). Although we acknowledge that these newly created TP_{in} tuning-points for the GS-10/GI-9, GS-9/GI-8, GS-8/GI-7 and GS-7/GI-6 transitions are based on the assumption of a similar synchronous marine SST and ice core $\delta^{18}O$ increase, we argue that the isochrons provide enough evidence to justify this choice. However, as the marine record does not completely cover the GS-10 to GI-9 time-interval, a small modification for this transition is made and it is assumed that the maximum marine SST value corresponds to the age of the maximum ice core $\delta^{18}O$ value (Fig. 9c; Table 4). Furthermore, it is important to point out that if the ARM/SST-based tuning-points, which constrain the interstadial-stadial transitions, are not replaced, the sedimentation-rate during GI-9 would be unrealistically high. The latter requires us to create an additional set of tuning-points for which we, unfortunately, rely on scarce
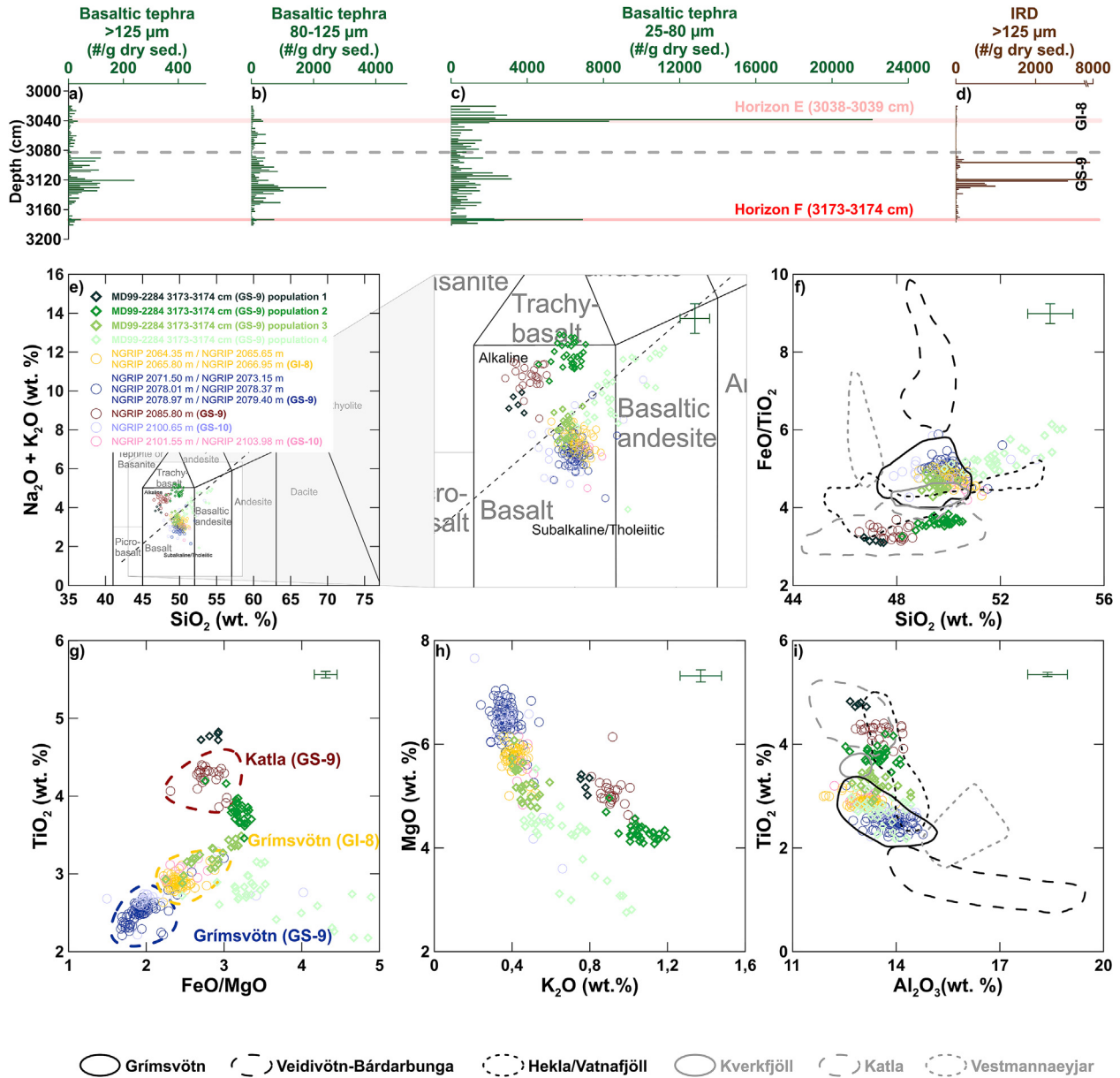
Fig. 8. Summary of Horizon F (3173−3174 cm). a-c) Tephrostratigraphy for selected depth-interval 4 (3020−3180 cm) with basaltic tephra shard concentrations for the different size fractions. Note: high-resolution areas are visible when there is no space left between the green bars. d) IRD concentrations. e-i) Comparison between the major elements of Horizon F (green diamonds) and stratigraphically fitting Greenland ice core horizons (NGRIP) from GI-8, GS-9 and GS-10 (open circles) (Bourne et al., 2013). All data are normalized to an anhydrous basis (i.e. 100% total oxides). Error bars are representing 2 standard deviations of replicate analyses of the BCR2g reference glass. e) Total alkalis vs. silica diagram (Le Bas et al., 1986). The dashed line indicates the boundary between the alkaline and subalkaline/tholeiitic series (MacDonald and Katsura, 1964). f) SiO_2 vs. FeO/TiO_2 biplot. g) FeO/MgO vs. TiO_2 biplot. h) K_2O vs. MgO biplot. i) Al_2O_3 vs. TiO_2 biplot. The different geochemical fields for Icelandic source volcanoes are based on glass analyses shown in Abbott et al. (2018a) and references within (here presented in plots f and i) and shown in Bourne et al. (2015) (here presented in plot g). (For interpretation of the references to color in this figure legend, the reader is referred to the Web version of this article.)

information regarding the temporal evolution of marine and ice core proxy data. However, one of the most well-known tephra layers and isochrons (i.e. NAAZ II) has been recorded in both North Atlantic marine and Greenland ice core climate archives at the interstadial-stadial transition of DO-15. Furthermore, based on the records of the relative abundance of *Neogloboquadrina pachyderma* (sinistral) and GISP $\delta^{18}O$, it was previously argued that the recordings of NAAZ II indicated a synchronous climatic transition from interstadial to stadial (Austin et al., 2004). And thus, again based on information derived from a tephra isochron, marine foraminiferal assemblages and ice core $\delta^{18}O$, we similarly assume that all interstadial-stadial transitions occurred in a consistent

manner with synchronous behavior of marine SST and ice core $\delta^{18}O$. Therefore, equivalent to the first set of tuning-points (TP_{in}), a second set (TP_{out}) is created. In particular, the TP_{out} set is produced by correlating the onset of the marine SST decrease to the start of the ice core $\delta^{18}O$ decrease (Fig. 9c; green crosses; Table 4).

Using the four independent isochrons (i.e. cryptotephra time-parallel markers) and tuning-points (i.e. TP_{in} & TP_{out}) instead of the ARM/SST-based tuning-points from Sadatzki et al. (2019) (Table 4), a synchronization of a marine and ice core palaeo-record spanning ca. 32−40 ka b2k is successfully realized and results in a refined age model for MD99-2284 (Fig. 9d). The tephra correlations form the independent foundation which, in addition,

Table 4
Summary of the tuning-points used in the refined MD99-2284 age model presented in this study. For each tuning-point the label (including depth), correlating NGRIP age including maximum counting error (MCE) (Andersen et al., 2006) and tuning method is provided. *This Age represents the average age and MCE for the four GI-8 horizons (i.e. 38.041 $\pm$ 1.441 ka b2k; 38.081 $\pm$ 1.441 ka b2k; 38.086 $\pm$ 1.442 ka b2k and 38.121 $\pm$ 1.445 ka b2k (see Table 3)). In addition, as a reference, for each of the identified isochrons, the previously published ages of Sadatzki et al. (2019) are given.

Climatic event	MD99-2284 Tuning-points	NGRIP Age $\pm$ MCE (ka b2k)	Tuning method	Sadatzki et al. (2019) Age (ka b2k)
GI-5/GS-5	MD99_2060.5 cm	32.067 $\pm$ 1.108	TP$_{out}$ (SST$_{out}$ $\downarrow$ = $\delta^{18}O_{out}$ $\downarrow$)	31.969
GI-5	**MD99_2109.5 cm**	**32.463 $\pm$ 1.130**	**Tephra isochron (Kverkfjöll)**	**32.404**
GS-6	**MD99_2134.5 cm**	**32.522 $\pm$ 1.132**	**Tephra isochron (Katla)**	**32 627**
GI-6/GS-6	MD99_2250.5 cm	33.363 $\pm$ 1.191	TP$_{out}$ (SST$_{out}$ $\downarrow$ = $\delta^{18}O_{out}$ $\downarrow$)	33.449
GI-6	**MD99_2322.5 cm**	**33.686 $\pm$ 1.207**	**Tephra isohchron (Kverkfjöll)**	**33.670**
GS-7/GI-6	MD99_2355.5 cm	33.759 $\pm$ 1.215	TP$_{in}$ (SST$_{in}$ $\uparrow$ = $\delta^{18}O_{in}$ $\uparrow$)	33.823
GI-7/GS-7	MD99_2540.5 cm	34.785 $\pm$ 1.288	TP$_{out}$ (SST$_{out}$ $\downarrow$ = $\delta^{18}O_{out}$ $\downarrow$)	34.911
GS-8/GI-7	MD99_2695.5 cm	35.526 $\pm$ 1.323	TP$_{in}$ (SST$_{in}$ $\uparrow$ = $\delta^{18}O_{in}$ $\uparrow$)	35.592
GI-8/GS-8	MD99_2854.5 cm	36.646 $\pm$ 1.401	TP$_{out}$ (SST$_{out}$ $\downarrow$ = $\delta^{18}O_{out}$ $\downarrow$)	36.878
GI-8	**MD99_3038.5 cm**	**38.081 ($\pm$0.040) $\pm$1.443***	**Tephra isochron (Grímsvötn)**	**37.943**
GS-9/GI-8	MD99_3085.5 cm	38.247 $\pm$ 1.450	TP$_{in}$ (SST$_{in}$ $\uparrow$ = $\delta^{18}O_{in}$ $\uparrow$)	38.226
GI-9/GS-9	MD99_3225.5 cm	39.928 $\pm$ 1570	TP$_{out}$ (SST$_{out}$ $\downarrow$ = $\delta^{18}O_{out}$ $\downarrow$)	40.023
GS-10/GI-9	MD99_3302.5 cm	40.108 $\pm$ 1577	TP$_{in}$ (SST$_{in}$ Max. = $\delta^{18}O_{in}$ Max.)	40.198

underpins the necessarily made (climatic) assumptions.

5. Discussion

5.1. Independent confirmation of the ARM/SST-tuning approach

The independent cryptotephra evidence is not only key for the synchronization of the disparate climate archives (Fig. 9d), it also confirms the validity and robustness of previously published age models based on an ARM/SST-tuning approach (Dokken et al., 2013; Sadatzki et al., 2019) (Fig. 10a–b). Despite small differences, both previously published studies tuned the marine ARM variations to the GS/GI-cycles as observed in the Greenland ice core δ^{18}O-signal. Based on previous work by Kissel et al. (1999, 2008), they assumed that the variations in those parameters change simultaneously, however, they selected slightly different tuning-points. Whereas Dokken et al. (2013) directly matched the rapid transitions, Sadatzki et al. (2019) refined the latter by applying a change point analysis to the ARM and SST records in order to derive change point probabilities more objectively. The latter resulted in more gradual changes within the ARM record, particularly throughout a stadial-interstadial transition (Fig. 10b). However, by using the independent isochrons, the onset and duration of the stadial-interstadial transitions are more tightly constrained which resolves some of the uncertainties regarding the progress of ARM changes (Fig. 10a). For the stadial-interstadial transitions, this study provides new and unique evidence for the relationship between the marine ARM and ice core δ^{18}O development. In particular, this new evidence argues for a well-pronounced synchronous and sharp stadial-interstadial transition (Fig. 10a–b). Hence, the independent cryptotephra time-parallel markers clearly support the original conclusion of Kissel et al. (1999, 2008). This study provides convincing evidence demonstrating the veracity of tuning North Atlantic magnetic records to Greenland ice core δ^{18}O to synchronize disparate climate archives.

5.2. Implications for the proxy data

The independent refinement and verification of the existing chronology might not appear to be a significant change, however, the new tephra-based synchronization has far-reaching implications for the interpretation of the various MD99-2284 proxy records. In particular, the time-parallel markers constraining the past abrupt climatic changes provide crucial information regarding the timing and phasing of events.

5.2.1. Sequence of climatic events

This tephra-based synchronization sheds a new perspective on the sequence of, and the phasing between, oceanic and atmospheric events. In order to identify any leads, lags or synchronicity, the main proxy records are displayed versus the new tephra-based age model of this study (Fig. 10). To show the advance provided by this refined age model, the same proxies are also plotted versus the chronology of Sadatzki et al. (2019) (Fig. 10). These proxy records represent, in the most simplistic and/or straightforward interpretation, ocean circulation (MD99-2284 ARM; Dokken et al., 2013) (Fig. 10a–b), sea ice cover (MD99-2284 P$_B$IP$_{25}$; Sadatzki et al., 2019) (Fig. 10c–d; Note the reversed y-axis), near-surface temperature (MD99-2284 SST; Dokken et al., 2013) (Fig. 10e–f), and atmospheric temperature (NGRIP δ^{18}O; Andersen et al., 2004, 2006; Seierstad et al., 2014) (Fig. 10a–f). Based on a general interpretation of the recognized pattern in all four DO-events, a simplified sequence of events during a GS/GI-cycle is presented (Fig. 10). In this schematic representation, the changes in NGRIP δ^{18}O (dark blue) and in the MD99-2284 proxy records (light blue) are visualized on top of a zoomed plot of the GS-9 to GI-8 transition (Fig. 10). The GI to GS transitions are characterized by a sharp decrease in atmospheric temperature, ocean circulation and near-surface temperature while a coinciding increase of sea ice cover occurs. These transitions are followed by a period of stable atmospheric temperature, sea ice cover and near-surface temperature, while the strength in ocean circulation still diminishes (Fig. 10 (1)). Throughout the GS, the atmospheric temperature remains constant and rather low. The first parameter to change is the near-surface temperature showing
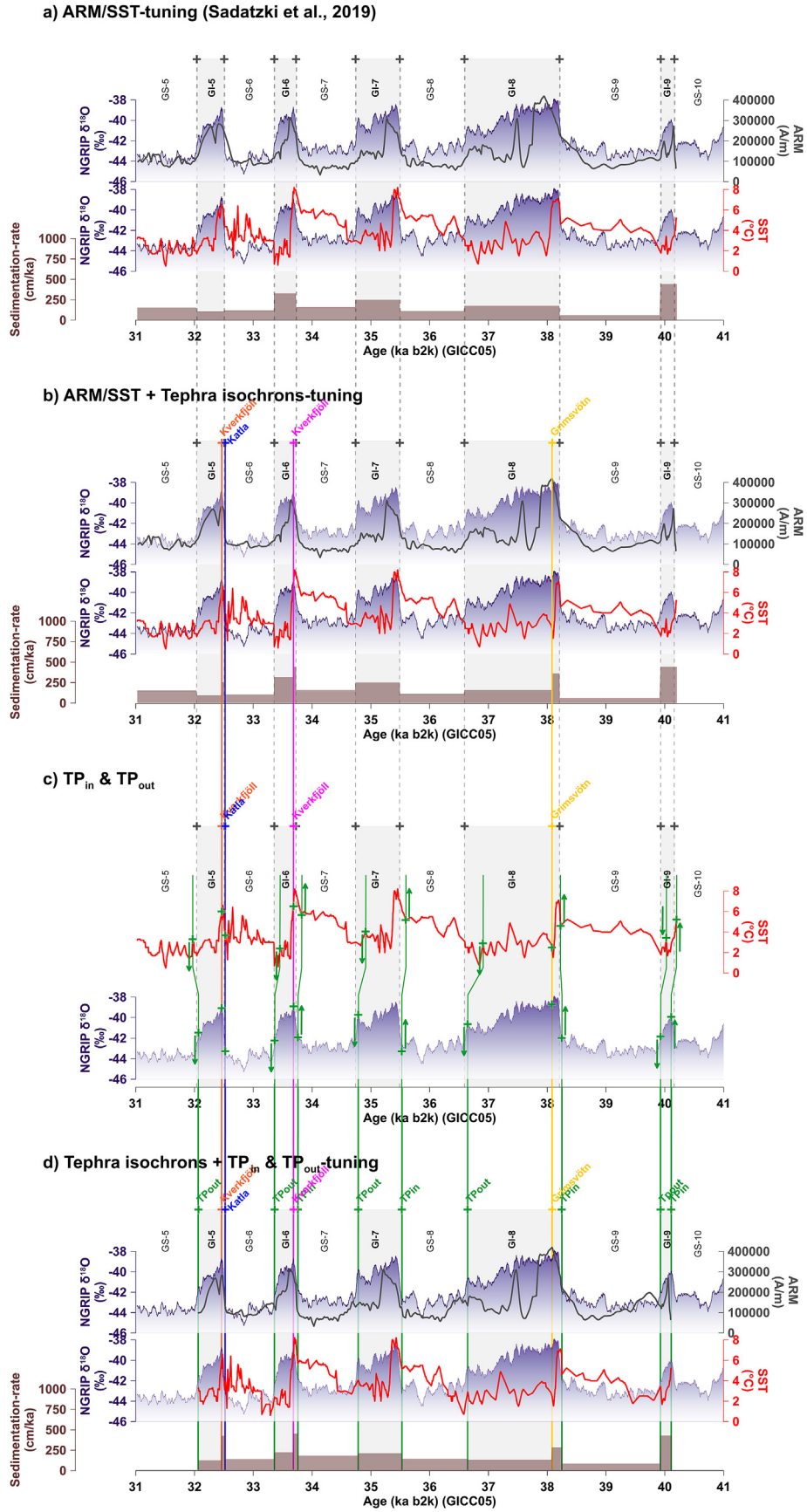
Fig. 9. Tephra-based synchronization and age model refinement of MD99-2284. For panel a, b and d, both ARM (dark grey) and SST (red) of MD99-2284 (Dokken et al., 2013) are plotted on top of NGRIP δ18O (purple) (Andersen et al., 2004, 2006; Seierstad et al., 2014). In addition, for each step in the age model refinement (panel a, b and d), the

a sharp significant increase (Fig. 10 (2)) followed by stable warmer temperatures potentially reflecting subsurface warming and/or stronger inflow of Atlantic water (Fig. 10 (3)). This near-surface temperature change in the ocean is quickly followed by a period during which the ocean circulation was more stable and the sea ice cover gradually started to decrease (Fig. 10 (4)). Subsequently, the GS to GI transition is characterized by a synchronous and drastic change in all parameters (Fig. 10 (5)). At this point in time, a strong and short-lived near-surface temperature overshoot is observed (see 5.2.2.) prior to stable and lower values for the remainder of the GI (Fig. 10 (6)). While the atmospheric temperature shows a gradual decrease throughout the GI, the ocean circulation seems to decrease in a two-phased pattern (Fig. 10 (7)). Eventually, at the end of the GI, the transition again occurs sharply for all parameters at the same time (Fig. 10 (8)). Although the stadial and interstadial transitions occur simultaneously throughout both those stages of a DO-event, these synchronized proxy records argue for initial changes within the ocean, supporting earlier findings (Sadatzki et al., 2019). This establishes the timing and phasing of proxy signals, which will help unravel the dynamics of DO-events. However, disentangling those dynamics in any detail does not lie within the scope of this study and thus, will not be discussed further.

5.2.2. Temperature overshoot duration

Within the near-surface temperature (SST) record, an overshoot (i.e. an abrupt and sharp temperature rise and subsequent decline by ca. 3 °C) is observed at the onset of each interstadial (Fig. 11: red and black highlighted bars). This so-called temperature overshoot is a characteristic feature of the interstadial periods and thus, with the overarching aim of understanding the dynamics of these events, it is important to constrain their timing. Based on the tephra-based synchronization presented in this study, the peak-duration of each interstadial temperature overshoot between GI-5 and GI-8 can now be estimated with high precision (Fig. 11; Table 5). However, note that within GI-7, the interstadial temperature overshoot is not constrained by a tephra horizon (Fig. 11a), which most likely explains why the duration of this particular temperature overshoot is about 100 years longer than those of GI-5, GI-6 and GI-8 (Table 5). Hence, excluding GI-7 enables us to estimate the average peak-duration of interstadial temperature overshoots as approximately 136 years. A comparison with previously published MD99-2284 chronologies demonstrates the advance (i.e. a high precision estimation) of this tephra-based synchronization. For example, the here estimated approximate duration (Fig. 11a; Table 5) is slightly longer than the <100 years previously proposed by Dokken et al. (2013) and about 100 years shorter than the interstadial temperature overshoot duration that would result from the chronology presented by Sadatzki et al. (2019) (Fig. 11b; Table 5). As the rapid interstadial temperature overshoot is an important feature for future proxy and model-based studies investigating the dynamics of DO-events, these estimated durations evidenced from our new tephra constraints are an important new finding.

5.3. Improving the North Atlantic tephra framework

Without marine sediment core MD99-2284, there are only two existing isochrons linking North Atlantic marine and Greenland ice core records between ca. 25 and 60 ka b2k (see 1.). However, with the well-targeted high-resolution investigation of MD99-2284, four new ice-marine time-parallel markers were identified. Thus, the results of this study triples the amount of existing isochrons between the marine and ice core archives between ca. 25 and 60 ka b2k. More specifically, this study presents four new ice-marine time-parallel markers that fall within a time-span of less than ca. 8000 years. This is, thus far, the shortest time-interval ever constrained by independent tephra isochrons in the North Atlantic during the Last Glacial Period. This study delivers a major contribution to the previously established North Atlantic tephra framework (Abbott et al., 2018a). In addition to these four independent isochrons and key horizons for future correlations, this study further expands the North Atlantic tephra framework by one rhyolitic cryptotephra horizon associated with the Katla volcanic system and interpreted as a Vedde-type tephra (i.e. Horizon D; Fig. 6g; see 3.2.4). The Vedde Ash was first recorded within western Norwegian lake sediments (Mangerud et al., 1984) and afterwards detected over a wide geographical area (e.g. Johansen et al., 1985; Svendsen and Mangerud, 1990; Bondevik et al., 1999; Sønstegaard et al., 1999; Wastegård et al., 2000; Mortensen et al., 2005; Lohne et al., 2007; Vorren et al., 2009; Lane et al., 2012). In addition, several tephra layers containing a similar geochemistry have been described in both terrestrial and marine records (e.g. Wastegård, 2002; Koren et al., 2008; Matthews et al., 2011; Abbott et al., 2016). These so-called Vedde-type tephras such as the Suduroy tephra (ca. 8 ka BP) (Wastegård, 2002), the AF555 tephra (ca. 11.2−11.8 ka BP) (Matthews et al., 2011) and the Dimna Ash (>15 ka BP) (Koren et al., 2008) are deposited, at least stratigraphically, close in time with the Vedde Ash (ca. 12.1 ka BP) (Rasmussen et al., 2006). Contrary, the Vedde-type tephra layer recorded within this study is much older (GI-7) (Table 2). This significant finding provides, together with a similar marine recording during DO-9 by Abbott et al. (2016), new insights into the evolution of the Katla volcanic system much further back in time. Nonetheless, Horizon D has the potential to act as a useful isochron, or time-parallel marker, for future correlations once the same horizon can be detected in other disparate and/or different climate archives.

Furthermore, this study also confirms that a high sedimentation-rate marine sediment core, as previously recommended by Bourne et al. (2013) and Griggs et al. (2014), enables the stratigraphical separation of the closely-spaced NGRIP GI-8 and GS-9 horizons that are all associated with the geochemical composition of the marine FMAZ III deposit. Although representing the same isochron as previously presented by Sadatzki et al. (2019), Horizon E is now placed on a stratigraphically refined position (i.e. MD99-2284_3038.5 cm). This is the only existing marine tephra layer associated with the FMAZ III deposit that is correlated to a disentangled part (i.e. the NGRIP GI-8 horizons) from the series of closely eruptive events described by Bourne et al. (2013). In comparison with the previously recorded amalgamation of material within marine sediments reflecting the full range of the closely timed Grímsvötn-sourced layers associated with FMAZ III (Rasmussen et al., 2003; Wastegård et al., 2006; Griggs et al., 2014; Abbott et al., 2016, 2018a), this result is a quite unique and promising advancement regarding cryptotephra studies in high

sedimentation-rates (brown) based on the corresponding age model is presented. The light grey highlighted areas represent the Greenland Interstadials (GI) 5−9. a) ARM/SST-tuning by Sadatzki et al. (2019). The grey crosses at the top of the panel and continuing grey dotted lines visualize the placing of the ARM/SST-based tuning-points. b) ARM/SST + Tephra isochrons-tuning as an in-between step within age model refinement of MD99-2284. The grey and colored crosses at the top of the panel and continuing grey dotted and colored full lines visualize the placing of the ARM/SST-based tuning-points and tephra isochrons, respectively. c) Visualization of the TP_{in} & TP_{out} based on assumptions 1 (i.e. $SST_{in} \uparrow = \delta^{18}O_{in} \uparrow$) and 2 (i.e. $SST_{out} \downarrow = \delta^{18}O_{out} \downarrow$), respectively. d) Tephra isochrons + TP_{in} & TP_{out}-tuning as the, in this study, proposed synchronization and refined age model of MD99-2284. The colored and green crosses at the top of the panel and colored and green full lines visualize the placing of the tephra isochrons and TP_{in} & TP_{out} tuning-points, respectively. (For interpretation of the references to color in this figure legend, the reader is referred to the Web version of this article.)
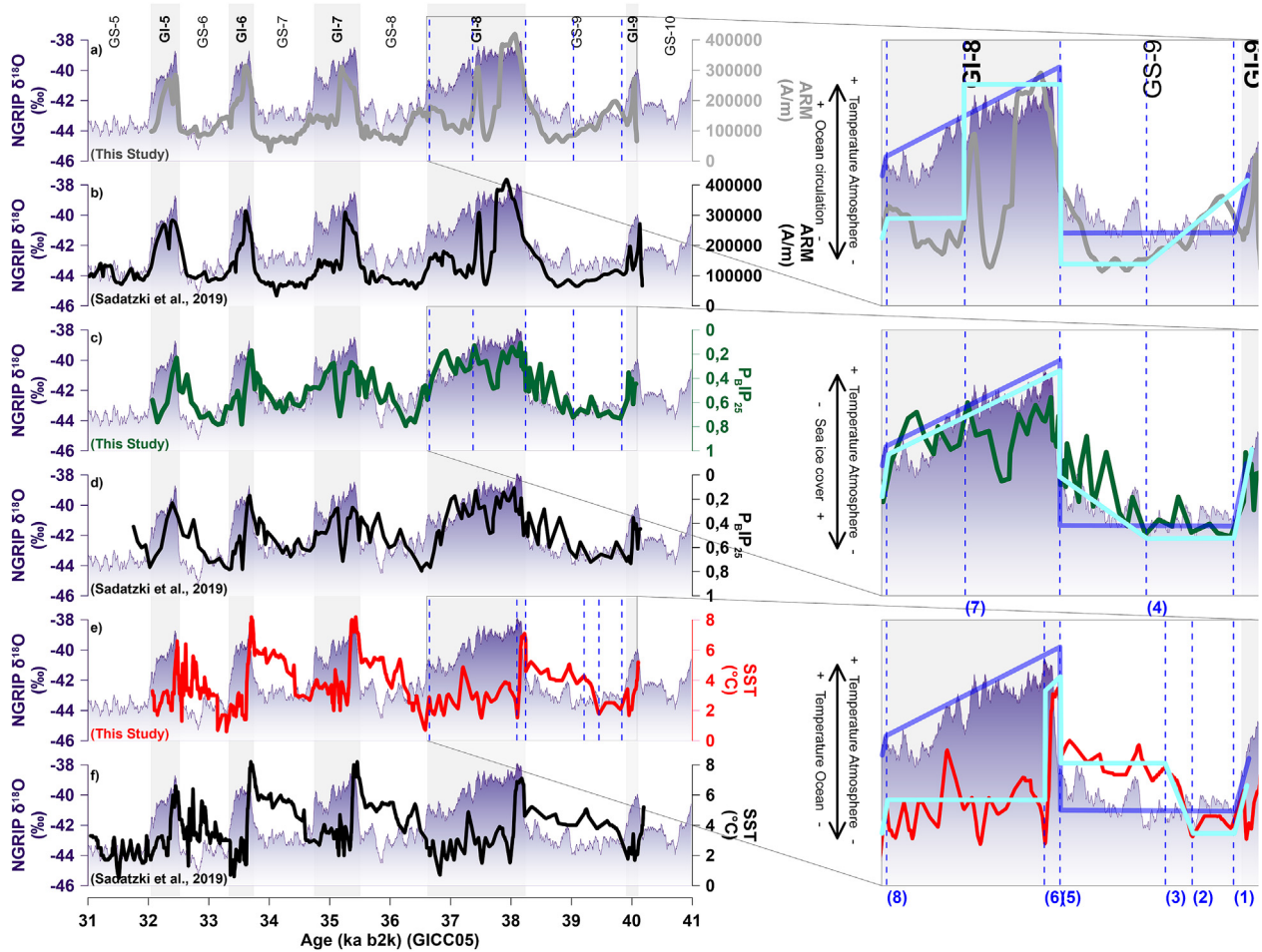
Fig. 10. Overview of main proxy records versus the tephra-based synchronization presented in this study. The light grey highlighted areas represent the Greenland Interstadials (GI) 5–9. The light blue lines visualize a simplified interpretation of the recognized pattern in the sequence of events during a single GS/GI-cycle (zoom). a-b) The ARM of MD99-2284 (Dokken et al., 2013) plotted versus a) the refined age model of this study (grey) and b) the age model of Sadatzki et al. (2019) (black). c-d) The P_BIP_{25} index of MD99-2284 (Sadatzki et al., 2019) plotted versus c) the refined age model of this study (green) and d) the age model of Sadatzki et al. (2019) (black). e-f) The SST of MD99-2284 (Dokken et al., 2013) plotted versus e) the refined age model of this study (red) and f) the age model of Sadatzki et al. (2019) (black). a-f) NGRIP $\delta^{18}O$ (purple) (Andersen et al., 2004, 2006; Seierstad et al., 2014). (For interpretation of the references to color in this figure legend, the reader is referred to the Web version of this article.)

sedimentation-rate core sites such as MD99-2284. Nonetheless, even in this marine sediment core, the complexity regarding FMAZ III remains partially unresolved as is shown by Horizon F's heterogeneous geochemistry.

Finally, despite it being well-known that many other marine records within the proximity of the core site have provided some of the highest identified tephra shard concentrations of the North Atlantic (e.g. Brendryen et al., 2010; Wastegård and Rasmussen, 2014; Griggs et al., 2014; Abbott et al., 2016, 2018a), not a single horizon identified in this study has previously been discovered in any of these marine crypto- and visible tephra investigations. This might be explained by a number of factors such as 1) the tephra horizons were not deposited at these locations in the first place, 2) the specific time-intervals were not investigated, 3) the previously investigated size fractions were too big or 4) the previously investigated resolutions were too low.

More specifically, it could be possible that due to a rather constrained dispersal area of the respective volcanic eruptions, tephra shards have never reached any of the other core sites nearby. Still, as these horizons reached the Greenland ice sheet, the dispersal areas were most likely widespread. Additionally, due to the proximity of Iceland, it seems rather unlikely that volcanic ash from these eruptions was not dispersed towards the regions nearby our

core site and other difficulties must explain the lack of shards. For example, the detection of single events might have been impossible due to differences in sedimentation-rates. In particular, when many eruptions occurred close in time (e.g. the previously described complexity regarding FMAZ III), the stratigraphic separation of these events might be unattainable. Furthermore, the investigated time-intervals for those previous studies have often been different and/or much larger compared to the rather short period in this study (i.e. ca. 8000 years). In addition, the here investigated time-interval falls between, previously recorded within multiple marine sediment cores, well-known isochrons and/or profoundly larger volcanic events such as FMAZ II and FMAZ IV (e.g. Rasmussen et al., 2003; Wastegård et al., 2006; Griggs et al., 2014; Wastegård and Rasmussen, 2014) as well as NAAZ II (e.g. Kvamme et al., 1989; Austin et al., 2004; Wastegård et al., 2006; Austin and Abbott, 2010; Brendryen et al., 2010). The focus of these previous studies might have been placed on larger time-periods where the need for these smaller volcanic events as independent time-parallel markers was less necessary. Additionally, many of these previous studies focused on tephra concentrations within a >150 μm size fraction and could have easily missed the here presented horizons as they were particularly pronounced within the fine-grained fraction (i.e. 25-80 μm). Hence, a specific cryptotephra
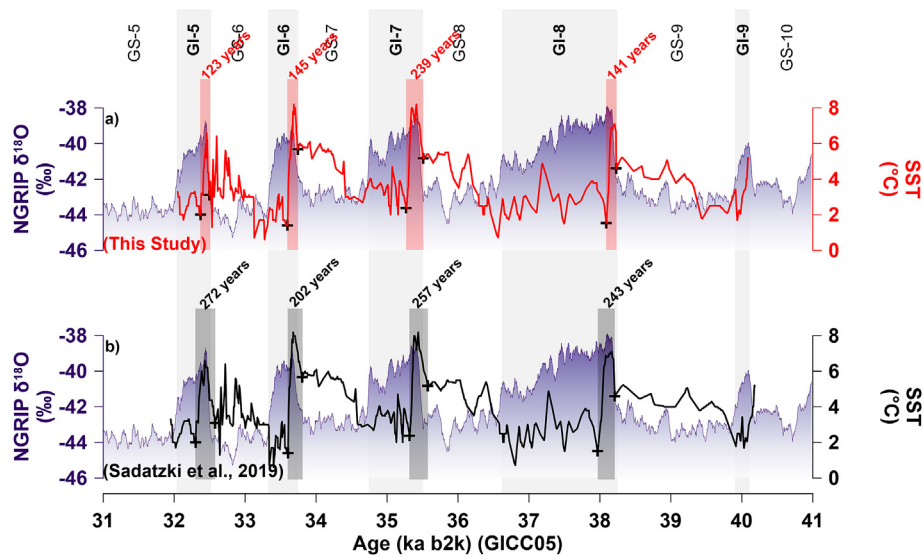
Fig. 11. Visual overview of the peak-duration of each interstadial temperature overshoot (highlighted boxes and numbers). The temperature overshoot is defined between the start and end of the sharp temperature rise and decline, respectively. The SST of MD99-2284 (Dokken et al., 2013) plotted versus a) the refined age model of this study (red) and b) the age model of Sadatzki et al. (2019) (black), in addition to NGRIP $\delta^{18}O$ (purple) (Andersen et al., 2004, 2006; Seierstad et al., 2014). (For interpretation of the references to color in this figure legend, the reader is referred to the Web version of this article.)

Table 5
The peak-duration of each interstadial temperature overshoot within this study is given in depth and age. The temperature overshoot is defined between the start and end of the sharp temperature rise and decline, respectively. The duration in age is calculated for the previously published age model (ARM/SST-tuning) by Sadatzki et al. (2019) and the refined chronology presented in this study (Tephra isochrons + TP_{in} & TP_{out}-tuning).

Climatic event	Temperature overshoot	MD99-2284 Depth (cm)	ARM/SST Age (ka b2k) Sadatzki et al. (2019)	Tephra isochrons + TP_{in} & TP_{out} Age (ka b2k) This study
GI-5	Start	2130.5	32.592	32.513
	End	2100.5	32.320	32.390
	Duration	30	0.272	**0.123**
GI-6	Start	2355.5	33.823	33.759
	End	2306.5	33.621	33.614
	Duration	49	0.202	**0.145**
GI-7	Start	2695.5	35.592	35.526
	End	2645.5	35.335	35.287
	Duration	50	0.257	0.239
GI-8	Start	3085.5	38.226	38.247
	End	3045.5	37.983	38.106
	Duration	40	0.243	**0.141**

investigation following a methodology including density and magnetic separation techniques (Griggs et al., 2014; Abbott et al., 2018b) is obviously crucial in order to discover some of the smaller eruptions through time. This has been demonstrated for the marine frameworks (e.g. Griggs et al., 2014; Abbott et al., 2016, 2018a) and hereby, verified by this study. Nonetheless, there is still a major difference between this study and previous cryptotephra investigations in the marine realm (e.g. Griggs et al., 2014; Abbott et al., 2016, 2018a). In particular, these previous studies initially applied a low-resolution (5 cm depth-intervals) approach covering wide core sections, in contrast to the well-targeted high-resolution approach utilised here. Due to the integration of sediment from several centimetres, it is likely that they might not have detected small events depositing low concentrations of tephra shards at the site due to dilution.

Thus, despite a variety of possible reasons, we argue that the here applied well-targeted high-resolution cryptotephra investigation of a high sedimentation-rate marine sediment core is the main reason to explain the different outcome from previous studies compared to this one. Therefore, despite the sediment availability,

time and financial considerations, this study highlights the importance of well-targeted high-resolution cryptotephra investigations in areas with an existing tephra framework. The latter approach has previously been advocated for by Timms et al. (2017) and discussed in Abbott et al. (2018a). Hence, this contribution to the North Atlantic tephra framework is not only important for future synchronization and correlation of disparate and/or distant climate archives, it most of all successfully demonstrates the use of cryptotephra as a geochronological tool in the marine environment.

6. Conclusions

The here presented well-targeted high-resolution cryptotephra investigation of marine sediment core MD99-2284, retrieved from the North Atlantic region, resulted in the discovery of six individual marine tephra horizons between ca. 32–40 ka b2k. The intensive investigation of the isochronous nature of each layer indicated that 5 out of 6 horizons possess the ability to act as an isochron. However, from those 5 horizons, one rhyolitic deposit cannot be linked to any existing Greenland ice core horizon and is, therefore, not

further used as a time-parallel marker in this study. Nonetheless, its geochemistry, associated with the Katla volcanic system, overlaps with published data of the Vedde Ash, which offers important new insights into the evolution of the Katla volcanic system. Additionally, this significant horizon still owns the future potential to operate as an isochron for correlations once the same horizon is traced in any other disparate and/or different climate archive. The remaining four tephra horizons possess an isochronous nature and are correlated to known Greenland ice core tephra deposits. Therefore, they are considered to represent independent time-parallel markers between the marine and ice realms. These four isochrons are, subsequently, used as independent cryptotephra time-parallel markers to synchronize MD99-2284 with the Greenland ice cores between ca. 32 and 40 ka b2k. Thereby, this synchronization provides the shortest time-interval (i.e. less than 8000 years) ever constrained by independent tephra isochrons in the North Atlantic during the Last Glacial Period and independently confirms the previously used marine ARM to ice core δ^{18}O tuning approach. Furthermore, it allowed the placement of a series of DO-events (i.e. DO-5 to DO-9) in the marine record on a solid chronological framework, which demonstrates a detailed phasing with atmospheric records from ice cores. The tephra-based constrain of the GS-6 to GI-5 transition by two separate isochrons delivers key evidence for synchronous oceanic and atmospheric climatic changes during the GS-GI transitions. Additionally, the timing of transitions and average peak-duration interstadial temperature overshoot is now estimated with high precision to approximately 136 years. Finally, the newly identified cryptotephra horizons and/or isochrons deliver an extremely important contribution to the North Atlantic tephra framework. In particular, including the four new isochrons from this study triples the amount of existing ice-marine time-parallel markers between ca. 25 and 60 ka b2k. As none of the MD99-2284 cryptotephra horizons were ever recorded before in the marine realm, this study successfully demonstrates the use of a well-targeted high-resolution cryptotephra investigation for geochronological purposes in the marine environment.

Author contributions

Sarah M.P. Berben: Conceptualization, Methodology, Formal analysis, Investigation, Writing - Original Draft, Writing - Review & Editing, Visualization. **Trond M. Dokken:** Conceptualization, Investigation, Resources, Writing - Review & Editing, Supervision. **Peter M. Abbott:** Methodology, Formal analysis, Investigation, Writing - Review & Editing, Visualization. **Eliza Cook:** Methodology, Investigation, Writing - Review & Editing. **Henrik Sadatzki:** Investigation, Writing - Review & Editing. **Margit H. Simon:** Investigation, Writing - Review & Editing. **Eystein Jansen:** Investigation, Resources, Writing - Review & Editing, Supervision, Funding acquisition.

Declaration of competing interest

The authors declare no competing interests.

Acknowledgments

Appendix A. Supplementary data

Supplementary data to this article can be found online at https://doi.org/10.1016/j.quascirev.2020.106277.

References

Abbott, P.M., Austin, W.E.N., Davies, S.M., Pearce, N.J.G., Hibbert, F.D., 2013. Cryptotephrochronology of a North East Atlantic marine sequence over termination II, the Eemian and the last interglacial-glacial transition. J. Quat. Sci. 28, 501–514.

Abbott, P.M., Austin, W.E.N., Davies, S.M., Pearce, N.J.G., Rasmussen, T.L., Wastegård, S., Brendryen, J., 2014. Re-evaluation and extension of the MIS 5 tephrostratigraphy of the Faroe Islands Region: the cryptotephras record. Palaeogeogr. Palaeoclimatol. Palaeoecol. 409, 153–168.

Abbott, P.M., Bourne, A.J., Purcell, C.S., Davies, S.M., Scourse, J.D., Pearce, N.J.G., 2016. Last glacial period cryptotephra deposits in an eastern North Atlantic marine sequence: exploring linkages to the Greenland ice-cores. Quat. Geochronol. 31, 62–76.

Abbott, P.M., Davies, S.M., Austin, W.E.N., Pearce, N.J.G., Hibbert, F.D., 2011. Identification of cryptotephra horizons in a north East Atlantic marine record spanning marine isotope stages 4 and 5a (∼60,000-82,000 a b2k). Quat. Int. 246, 177–189.

Abbott, P.M., Griggs, A.J., Bourne, A.J., Chapman, M.R., Davies, S.M., 2018a. Tracing marine cryptotephras in the North Atlantic during the last glacial period: improving the North Atlantic marine tephrostratigraphic framework. Quat. Sci. Rev. 189, 169–186.

Abbott, P.M., Griggs, A.J., Bourne, A.J., Davies, S.M., 2018b. Tracing marine cryptotephras in the North Atlantic during the last glacial period: protocols for identification, characterisation and evaluating depositional controls. Mar. Geol. 401, 81–97.

Andersen, K.K., Azuma, N., Barnola, J.-M., Bigler, M., Biscaye, P., Caillon, N., Chappellaz, J., Clausen, H.B., Dahl-Jensen, D., Fischer, H., Flückiger, J., Fritzsche, D., Fujii, Y., Goto-Azuma, K., Grønvold, K., Gundestrup, N.S., Hansson, M., Huber, C., Hvidberg, C.S., Johnsen, S.J., Jonsell, U., Jouzel, J., Kipfstuhl, S., Landais, A., Leuenberger, M., Lorrain, R., Masson-Delmotte, V., Miller, H., Motoyama, H., Narita, H., Popp, T., Rasmussen, S.O., Raynaud, D., Rothlisberger, R., Ruth, U., Samyn, D., Schwander, J., Shoji, H., Siggaard-Andersen, M.-L., Steffensen, J.P., Stocker, T., Sveinbjörnsdóttir, A.E., Svensson, A., Takata, M., Tison, J.-L., Thorsteinsson, T., Watanabe, O., Wilhelms, F., White, J.W.C., 2004. High-resolution record of Northern Hemisphere climate extending into the last interglacial period. Nature 431, 147–151.

Andersen, K.K., Svensson, A., Johnsen, S.J., Rasmussen, S.O., Bigler, M., Rothlisberger, R., Ruth, U., Siggaard Andersen, M.L., Steffensen, J.P., Dahl-Jensen, D., Vinther, B.M., Clausen, H.B., 2006. The Greenland ice core chronology 2005, 15-42 ka. Part 1: constructing the time scale. Quat. Sci. Rev. 25, 3246–3257.

Austin, W.E.N., Abbott, P.M., 2010. Comment: were last glacial climate events simultaneous between Greenland and France? A quantitative comparison using non-tuned chronologies. In: Blaauw, M., Wohlfarth, B., Christen, J.A., Ampel, L., Veres, D., Hughen, K., Preusser, F., Svensson, A. (Eds.), J. Quat. Sci. 25, 1045–1046, 2009.

Austin, W.E.N., Wilson, L.J., Hunt, J.B., 2004. The age and chronostratigraphical significance of North Atlantic ash zone ii. J. Quat. Sci. 19, 137–146.

Begét, J., Mason, O., Anderson, P., 1992. Age, extent and climatic significance of the c. 3400 BP Aniakchak tephra, western Alaska, USA. Holocene 2, 51–56.

Blockley, S.P.E., Lane, C.S., Hardiman, M., Rasmussen, S., Seierstad, I., Steffensen, J., Svensson, A., Lotter, A., Turney, C., Ramsey, C., 2012. Synchronisation of palaeoenvironmental records over the last 60,000 years, and an extended INTIMATE event stratigraphy to 48,000 b2k. Quat. Sci. Rev. 36, 2–10.

Blockley, S.P.E., Pyne-O'Donnell, S.D.F., Lowe, J.J., Matthews, I.P., Stone, A., Pollard, A.M., Turney, C.S.M., Molyneux, E.G., 2005. A new and less destructive

laboratory procedure for the physical separation of distal glass tephra shards from sediments. Quat. Sci. Rev. 24, 1952—1960.

Bond, G., Broecker, W., Johnsen, S., McManus, J., Labeyrie, L., Jouzel, J., Bonani, G., 1993. Correlations between climate records from North Atlantic sediments and Greenland ice. Nature 365, 143—147.

Bondevik, S., Birks, H.H., Gulliksen, S., Mangerud, J., 1999. Late Weichselian marine 14C reservoir ages at the western coast of Norway. Quat. Res. 52, 104—114.

Borchardt, G.A., Aruscavage, P.J., Millard Jr., H., 1972. Correlation of the Bishop ash, a Pleistocene marker bed, using instrumental neutron activation analysis. J. Sediment. Res. 42, 201—206.

Bourne, A.J., Cook, E., Abbott, P.M., Seierstad, I.K., Steffensen, J.P., Svensson, A., Fischer, H., Schupbach, S., Davies, S.M., 2015. A tephra lattice for Greenland and a reconstruction of volcanic events spanning 25-45 ka b2k. Quat. Sci. Rev. 118, 122—141.

Bourne, A.J., Davies, S.M., Abbott, P.M., Rasmussen, S.O., Steffensen, J.P., Svensson, A., 2013. Revisiting the Faroe Marine Ash Zone III in two Greenland ice cores: implications for marine-ice correlations. J. Quat. Sci. 28, 641—646.

Brendryen, J., Haflidason, H., Sejrup, H.P., 2010. Norwegian Sea tephrostratigraphy of marine isotope stages 4 and 5: prospects and problems for tephrochronology in the North Atlantic region. Quat. Sci. Rev. 29, 847—864.

Curry, W.B., Oppo, D.W., 1997. Synchronous, high-frequency oscillations in tropical sea surface temperatures and North Atlantic Deep Water production during the last glacial cycle. Paleoceanography 12, 1—14.

Dansgaard, W., Johnsen, S.J., Clausen, H.B., Dahl-Jensen, D., Gundestrup, N.S., Hammer, C.U., Hvidberg, C.S., Steffensen, J.P., Sveinbjörnsdóttir, A.E., Jouzel, J., Bond, G., 1993. Evidence for general instability of past climate from a 250-kyr ice core record. Nature 364, 218—220.

Davies, S.M., 2015. Cryptotephras: the revolution in correlation and precision dating. J. Quat. Sci. 30, 114—130.

Davies, S.M., Abbott, P.M., Meara, R.H., Pearce, N.J.G., Austin, W.E.N., Chapman, M.R., Svensson, A., Bigler, M., Rasmussen, T.L., Rasmussen, S.O., Farmer, E.J., 2014. A North Atlantic tephra framework for 130-60years b2k: new tephra discoveries, marine based correlations and future challenges. Quat. Sci. Rev. 106, 101—121.

Davies, S.M., Abbott, P.M., Pearce, N.J.G., Wastegård, S., Blockley, S.P.E., 2012. Integrating the INTIMATE records using tephrochronology: rising to the challenge. Quat. Sci. Rev. 36, 11—27.

Davies, S.M., Wastegård, S., Abbott, P.M., Barbante, C., Bigler, M., Johnsen, S.J., Rasmussen, T.L., Steffensen, J.P., Svensson, A., 2010. Tracing volcanic events in the NGRIP ice-core and synchronising North Atlantic marine records during the Last Glacial period. Earth Planet Sci. Lett. 294 (1—2), 69—79.

Davies, S.M., Wastegård, S., Rasmussen, T.L., Svensson, A., Johnsen, S.J., Steffensen, J.P., Andersen, K.K., 2008. Identification of the Fugloyarbanki tephra in the NGRIP ice core: a key tie-point for marine and ice-core sequences during the last glacial period. J. Quat. Sci. 23, 409—414.

Dokken, T.M., Jansen, E., 1999. Rapid changes in the mechanism of ocean convection during the last glacial period. Nature 401, 458—461.

Dokken, T.M., Nisancioglu, K.H., Li, C., Battisti, D.S., Kissel, C., 2013. Dansgaard-Oeschger cycles: interactions between ocean and sea ice intrinsic to the Nordic seas. Paleoceanography 28, 491—502.

Enache, M.D., Cumming, B.F., 2006. The morphological and optical properties of volcanic glass: a tool to assess density-induced vertical migration of tephra in sediment cores. J. Paleolimnol. 35, 661—667.

Griggs, A.J., Davies, S.M., Abbott, P.M., Rasmussen, T.L., Palmer, A.P., 2014. Optimising the use of marine tephrochronology in the north atlantic: a detailed investigation of the Faroe marine ash zones II, III and IV. Quat. Sci. Rev. 106, 122—139.

Griggs, A.J., Davies, S.M., Abbott, P.M., Coleman, M., Palmer, A.P., Rasmussen, T.L., Johnston, R., 2015. Visualising tephra sedimentation processes in the marine environment: the potential of X-ray microtomography. Geochem. Geophy. Geosy. 16 (12), 4329—4343.

Grönvold, K., Óskarsson, N., Johnsen, S.J., Clausen, H.B., Hammer, C.U., Bond, G., Bard, E., 1995. Ash layers from Iceland in the GRIP ice core correlated with oceanic and land sediments. Earth Planet Sci. Lett. 135, 149—155.

Hayward, C., 2012. High spatial resolution electron probe microanalysis of tephras and melt inclusions without beam induced chemical modification. Holocene 22, 119—125.

Hodder, A.P.W., Wilson, A.T., 1976. Identification and correlation of thinly bedded tephra: the Tirau and Mairoa ashes. N. Z. J. Geol. Geophys. 19, 663—682.

Hunt, J.B., Fannin, N.G.T., Hill, P.G., Peacock, J.D., 1995. The tephrochronology and radiocarbon dating of North Atlantic, late Quaternary sediments: an example from the St Kilda Basin. In: Scrutton, R.A., Stoker, M.S., Shimmield, G.B., Tudhope, A.W. (Eds.), The Tectonics, Sedimentation and Palaeoceanography of the North Atlantic Region, pp. 227—248. London.

Jennings, A., Thordarson, T., Zalzal, K., Stoner, J., Hayward, C., Geirsdóttir, Á., Miller, G., 2014. Holocene tephra from Iceland and Alaska in SE Greenland shelf sediments. In: Austin, W.E.N., Abbott, P.M., Davies, S.M., Pearce, N.J.G., Wastegård, S. (Eds.), Marine Tephrochronology, vol. 398. Geological Society London, Special Publications.

Johansen, O.I., Henningsmoen, K.E., Sollid, J.L., 1985. Deglaciation of Tingvollhalvøya and adjacent areas, Nordvestlandet, in light of the vegetation development (in Norwegian). Nor. Geografisk Tidsskr. 39, 155—174.

Kissel, C., Laj, C., Labeyrie, L., Dokken, T.M., Voelker, A., Blamart, D., 1999. Rapid climatic variations during marine isotopic stage 3: magnetic analysis of sediments from Nordic Seas and North Atlantic. Earth Planet Sci. Lett. 171, 489—502.

Kissel, C., Laj, C., Piotrowski, A.M., Goldstein, S.L., Hemming, S.R., 2008. Millennial-

scale propagation of Atlantic deep waters to the glacial Southern Ocean. Paleoceanography 23, PA2102.

Koren, J.H., Svensson, J.I., Mangerud, J., Furnes, H., 2008. The Dimna Ash - a 12.8 14C ka-old volcanic ash in Western Norway. Quat. Sci. Rev. 27, 85—94.

Kvamme, T., Mangerud, J., Furnes, H., Ruddiman, W., 1989. Geochemistry of pleistocene ash zones in cores from the north atlantic. Norsk Geologisk Tidskrift 69, 251—272.

Lackschewitz, K.S., Wallrabe-Adams, H.J., 1997. Composition and origin of volcanic ash zones in Late Quaternary sediments from the Reykjanes Ridge: evidence for ash fallout and ice rafting. Mar. Geol. 136, 209—224.

Lane, C.S., Blockley, S.P.E., Mangerud, J., Smith, V.C., Lohne, Ø.S., Tomlinson, E.L., Matthews, I.P., Lotter, A.F., 2012. Was the 12.1 ka Icelandic Vedde Ash one of a kind? Quat. Sci. Rev. 33, 87—99.

Le Bas, M.J., Le Maitre, R.W., Streckeisen, A., Zanettin, B., 1986. A chemical classification of volcanic rocks based on the Total Alkali Silica diagram. J. Petrol. 27, 745—750.

Lohne, Ø.S., Bondevik, S., Mangerud, J., Svendsen, J.I., 2007. Sea-level fluctuations imply that the Younger Dryas ice-sheet expansion in western Norway commenced during the Allerød. Quat. Sci. Rev. 26, 2128—2151.

Lowe, D.J., 2011. Tephrochronology and its application: a review. Quat. Geochronol. 6, 107—153.

Lowe, J.J., Rasmussen, S.O., Björck, S., Hoek, W.Z., Steffensen, J.P., Walker, M.J.C., Yu, Z.C., the INTIMATE group, 2008. Synchronisation of palaeoenvironmental events in the North Atlantic region during the Last Termination: a revised protocol recommended by the INTIMATE group. Quat. Sci. Rev. 27, 6—17.

MacDonald, G.A., Katsura, T., 1964. Chemical composition of Hawaiian lavas. J. Petrol. 5, 83—133.

Mangerud, J., Lie, S.E., Furnes, H., Kristiansen, I.L., Lømo, L., 1984. A younger dryas ash bed in western Norway, and its possible correlations with tephra in cores from the Norwegian sea and the north atlantic. Quat. Res. 21, 85—104.

Matthews, I.P., Birks, H.H., Bourne, A.J., Brooks, S.J., Lowe, J.J., Macleod, A., Pyne-O'Donnell, S.D.F., 2011. New age estimates and climatostratigraphic correlations for the Borrobol and penifiler tephras: evidence from abernethy forest, scotland. J. Quat. Sci. 26, 247—252.

Mortensen, A.K., Bigler, M., Gronvold, K., Steffensen, J.P., Johnsen, S.J., 2005. Volcanic ash layers from the last glacial termination in the NGRIP ice core. J. Quat. Sci. 20, 209—219.

Pearce, N.J.G., Abbott, P.M., Martin-Jones, C., 2014. Microbeam methods for the analysis of glass in fine grained tephra deposits: a SMART perspective on current and future trends. In: Austin, W.E.N., Abbott, P.M., Davies, S.M., Pearce, N.J.G., Wastegård, S. (Eds.), Marine Tephrochronology, vol. 398. Geological Society of London Special Publication.

Pearce, N.J.G., Alloway, B.V., Westgate, J.A., 2008. Mid-Pleistocene silicic tephra beds in the Auckland region, New Zealand: their correlation and origins based on the trace element analyses of single glass shards. Quat. Int. 178, 16—43.

Perkins, M.E., Brown, F.H., Nash, W.P., Williams, S.K., McIntosh, W., 1998. Sequence, age, and source of silicic fallout tuffs in middle to late Miocene basins of the northern Basin and Range province. Geol. Soc. Am. Bull. 110, 344—360.

Perkins, M.E., Nash, W.P., Brown, F.H., Fleck, R.J., 1995. Fallout tuffs of Trapper Creek, Idaho-a record of miocene explosive volcanism in the snake river plain volcanic province. Geol. Soc. Am. Bull. 107, 1484—1506.

Pilcher, J.R., Hall, V.A., 1992. Towards a tephrochronology for the Holocene of the north of Ireland. Holocene 2, 255—259.

Rasmussen, S.O., Andersen, K.K., Svensson, A.M., Steffensen, J.P., Vinther, B.M., Clausen, H.B., Siggaard-Andersen, M.L., Johnsen, S.J., Larsen, L.B., Dahl-Jensen, D., Bigler, M., Röthlisberger, R., Fischer, H., Goto-Azuma, K., Hansson, M.E., Ruth, U., 2006. A new Greenland ice core chronology for the last glacial termination. J. Geophys. Res. Atmos. 111 (D6).

Rasmussen, T.L., Wastegård, S., Kuijpers, A., van Weering, T.C.E., Heinemeier, J., Thomsen, E., 2003. Stratigraphy and distribution of tephra layers in marine sediment cores from the Faeroe Islands, North Atlantic. Mar. Geol. 199, 263—277.

Ruddiman, W.F., Glover, L.K., 1972. Vertical mixing of ice rafted volcanic ash in north Atlantic sediments. Geol. Soc. Am. Bull. 83, 2817—2836.

Sadatzki, H., Dokken, T.M., Berben, S.M.P., Muschitiello, F., Stein, R., Fahl, K., Menviel, L., Timmermann, A., Jansen, E., 2019. Sea ice variability in the southern Norwegian Sea during glacial Dansgaard-Oeschger climate cycles. Sci. Adv. 5, eaau6174.

Schlitzer, R., 2018. Ocean Data View. odv.awi.de.

Seierstad, I.K., Abbott, P.M., Bigler, M., Blunier, T., Bourne, A.J., Brook, E., Buchardt, S.L., Buizert, C., Clausen, H.B., Cook, E., Dahl-Jensen, D., Davies, S.M., Guillevic, M., Johnsen, S.J., Pedersen, D.S., Popp, T.J., Rasmussen, S.O., Severinghaus, J.P., Svensson, A., Vinther, B.M., 2014. Consistently dated records from the Greenland GRIP, GISP2 and NGRIP ice cores for the past 104 ka reveal regional millennial-scale d18O gradients with possible Heinrich event imprint. Quat. Sci. Rev. 106, 29—46.

Sønstegaard, E., Aa, A.R., Klakegg, O., 1999. Younger Dryas glaciation in the Alfoten area, western Norway; evidence from lake sediments and marginal moraines. Nor. Geol. Tidsskr. 79, 33—45.

Svendsen, J.I., Mangerud, J., 1990. Sea-level changes and pollen stratigraphy on the outer coast of Sunnmore, western Norway. Nor. Geol. Tidsskr. 70, 111—134.

Svensson, A., Andersen, K.K., Bigler, M., Clausen, H.B., Dahl Jensen, D., Davies, S.M., Johnsen, S.J., Muscheler, R., Rasmussen, S.O., Röthlisberger, R., Steffensen, J.P., Vinther, B.M., 2006. The Greenland ice core chronology 2005, 15—42 ka. Part 2: comparison to other records. Quat. Sci. Rev. 25, 3258—3267.

Timms, R.G.O., Matthews, I.P., Palmer, A.P., Candy, I., Abel, L., 2017. A high-resolution tephrostratigraphy from Quoyloo meadow, Orkney, Scotland: implications for the tephrostratigraphy of nw europe during the last glacial-interglacial transition. Quat. Geochronol. 40, 67–81.

Turney, C.S.M., 1998. Extraction of rhyolitic component of Vedde microtephra from minerogenic lake sediments. J. Paleolimnol. 19, 199–206.

Vorren, K.D., Elverland, E., Blaauw, M., Ravna, E.K., Jensen, C.A.H., 2009. Vegetation and climate c. 12 300e9000 cal. yr BP at Andøya, NW Norway. Boreas 38, 401–420.

Wallrabe-Adams, H.J., Lackschewitz, K.S., 2003. Chemical composition, distribution, and origin of silicic volcanic ash layers in the Greenland-Iceland Norwegian Sea: explosive volcanism from 10 to 300 ka as recorded in deep sea sediments. Mar. Geol. 19, 273–293.

Wastegård, S., Wohlfarth, B., Subetto, D.A., Sapelko, T.V., 2000. Extending the known distribution of the younger dryas Vedde ash into northwestern Russia. J. Quat. Sci. 15, 581–586.

Wastegård, S., 2002. Early to middle Holocene silicic tephra horizons from the Katla volcanic system, Iceland: new results from the Faroe Islands. J. Quat. Sci. 17, 723–730.

Wastegård, S., Rasmussen, T.L., 2014. Faroe Marine Ash Zone IV: a new MIS3 ash zone of the Faroe Islands margin. In: Austin, W.E.N., Abbott, P.M., Davies, S.M., Pearce, N.J.G., Wastegård, S. (Eds.), Marine Tephrochronology, vol. 398. Geological Society of London Special Publication.

Wastegård, S., Rasmussen, T.L., Kuijpers, A., Nielsen, T., van Weering, T.C.E., 2006. Composition and origin of ash zones from marine isotope stages 3 and 2 in the North atlantic. Quat. Sci. Rev. 25, 2409–2419.

Zielinski, G.A., Mayewski, P.A., Meeker, L.D., Whitlow, S., Twickler, M.S., 1996. A 110,000 year record of explosive volcanism from the GISP2 (Greenland) ice core. Quat. Res. 45, 109–118.